

A STUDY ON LIQUID-COOLED JACKETS FOR SYNCHRONOUS  
RELUCTANCE MOTORS AND APPLICATION OF MACHINE LEARNING IN  
COOLING STRATEGIES



HOANG KHAN NGUYEN

A THESIS SUBMITTED IN PARTIAL FULFILLMENT  
OF THE REQUIREMENT FOR THE DEGREE OF  
MASTER DEGREE OF ENGINEERING IN AUTOMOTIVE AND ADVANCED  
TRANSPORTATION ENGINEERING  
SCHOOL OF ENGINEERING  
KING MONGKUT'S INSTITUTE OF TECHNOLOGY LADKRABANG  
2024

KMITL-2024-EN-M- 277-262

This material is reserved for educational use only, not allowed for commercial use.

Forbidden to modify the content, and cite the document when use.



**COPYRIGHT 2024**

**SCHOOL OF ENGINEERING**

**KING MONGKUT'S INSTITUTE OF TECHNOLOGY LADKRABA**

This material is reserved for educational use only, not allowed for commercial use.

Forbidden to modify the content, and cite the document when use.

<b>Thesis</b>	A Study on Liquid-cooled Jackets for Synchronous Reluctance Motors and Application of Machine Learning in Cooling Strategies
<b>Student</b>	Mr. Hoang Khan Nguyen
<b>Student ID.</b>	65016114
<b>Degree</b>	Master of Engineering
<b>Program</b>	Automotive and Advanced Transportation Engineering
<b>Year</b>	2024
<b>Thesis Advisor</b>	Asst. Prof. Dr. Chinda Charoenphonphanich
<b>Co-Thesis Advisor</b>	Dr.-Ing. Manop Masomtob Prof. Shuichiro Hirai

### ABSTRACT IN ENGLISH

The prevalence of electric vehicles (EVs) is a near future that we can envision. As the driving force of EVs, the motor needs attention in its structure and safety systems, which require research. A motor with a well-functioning cooling system can operate in more adverse environments. In the system, there needs to be a balance between design and control systems, as an unstable control system, no matter how intelligent the design, will result in lower efficiency and vice versa. Therefore, the research objective includes assessing the factors affecting the cooling process, proposing a rational design, and applying an intelligent control method for the coolant flow. This study investigates and evaluates the factors affecting the cooling process through experimentation and simulation. The experimental process serves two primary purposes: collecting input parameters for the simulation step and validating the simulation results to ensure confidence. The simulation process is based on the step running technique, offering the advantages of fast computation and reduced computer memory usage. Machine learning (ML) is an intelligent water pump control method with 1000 cases of training data, including three key parameters: motor torque, flow rate, and inlet temperature. The results show that a water-cooling jacket can significantly reduce the temperature of the motor; the heat generation of the motor and the flow rate of water affect the maximum temperature and temperature

This material is reserved for educational use only, not allowed for commercial use.

Forbidden to modify the content, and cite the document when use.

fluctuation. This comprehensive validation method incorporates three types of validation: time-dependent validation, stable state validation of 3 key parameters, and temperature distribution validation. The topology of the water-cooling jacket (WJ) influences temperature difference, pressure drop, and temperature distribution. In term of control, ML models can directly determine the optimal flow rate and save pump capacity. An equation derived from a machine learning (ML) model functions as a motor cooling system to optimize memory and facilitate integration with other systems, even large systems like EVs. The accuracy of the equation was certificated by calibrating it with the ML model and checking its loss against experimental data, achieving R2 scores of 0.9901 and 0.9994, respectively. These results inferred that the error of the equation will increase as the boundary conditions deviate further from the actual experimental data. This equation is the initial step for generating a deep neural network (DNN) model to derive equations for various types of motors if the database for the training step is sufficient.

**Keywords:** water-cooling system, time-dependent validation, stable state validation, machine learning, MATLAB/Simulink, PID, activation function.

## ACKNOWLEDGEMENT

Firstly, I would like to express my gratitude to the TAIST-Tokyo Tech committee for selecting me and granting me the full scholarship opportunity to pursue a master's degree in automotive and advanced transportation engineering (A2TE) program.

I also want to express my gratitude to King Mongkut's Institute of Technology Ladkrabang for awarding me the Monozukuri degree scholarship, which supports me in covering living expenses and experimental material fees.

I also want to express my gratitude to my main advisor in research, Asst. Prof. Dr. Chinda Charoenphonphanich, from King Mongkut's Institute of Technology Ladkrabang. His dedication has always supported me through all the challenges of study and research. His invaluable contributions during our meetings have greatly aided me.

I sincerely want to express my deepest gratitude to Dr.-Ing. Manob Masomtob, my co-advisor from the National Energy Technology Center (ENTEC), National Science and Technology Development Agency (NSTDA). His knowledge and experience have been invaluable contributions to all of my research results.

I also want to extend my deepest gratitude to Dr. Burin Kerdesup, my co-advisor, from the National Electronics and Computer Technology Center (NECTEC), National Science and Technology Development Agency (NSTDA). His support in the experimental system and insightful feedback have contributed significantly to my journey in pursuing this master's degree. I am also deeply grateful to Mr. Santipong Karukanan and Mr. Prasit Champa from NECTEC for their sincere assistance throughout the process of experimental setup and testing conduction.

I would like to express my gratitude to Prof. Shuichiro Hirai, my co-advisor from Tokyo Institute of Technology. I have learned a great deal from him during his visits and teaching in Thailand.

I would like to thank Mr. Jedsada Tangmongkhonsuk, my lab mate. His assistance to a foreigner like me is highly appreciated. Thanks to him, I was able to complete my experiments on schedule.

Lastly, I would like to thank my parents for their unwavering support throughout this journey.

Hoang Khan Nguyen

This material is reserved for educational use only, not allowed for commercial use.

Forbidden to modify the content, and cite the document when use.

# TABLE OF CONTENTS

	Page
ABSTRACT IN ENGLISH.....	I
ACKNOWLEDGEMENT .....	III
TABLE OF CONTENTS .....	IV
LIST OF TABLES .....	VII
LIST OF FIGURES.....	VIII
LIST OF AND SYMBOLS .....	X
LIST OF ABBREVIATIONS .....	XII
CHAPTER 1 INTRODUCTION .....	1
1.1 RESEARCH BACKGROUND.....	1
1.2 GOALS AND OBJECTIVES .....	1
1.3 SCOPE OF WORK.....	2
1.4 OUTLINE OF THESIS .....	3
CHAPTER 2 LITERATURE REVIEW.....	5
2.1 SYNCHRONOUS RELUCTANCE MACHINE .....	5
2.2 TYPES OF COOLING METHOD .....	6
2.3 ADVANTAGE OF MACHINE LEARNING .....	9
2.4 VEHICLE DYNAMICS .....	10
2.4.1 Aerodynamic Resistance .....	11
2.4.2 Grade Resistance.....	12
2.4.3 Rolling Resistance .....	12
2.4.4 Inertial resistance .....	13
2.4.5 Lift Force .....	13
2.5 ABSOLUTE AND RELATIVE ERROR .....	13
CHAPTER 3 PART 1: EFFECT OF FACTORS ON COOLING PROCESS .....	15
3.1 COLLECTING INPUT PARAMETERS.....	15
3.2 RESULTS AND DISCUSSION .....	19
3.2.1 Torque and Heat Generation of Motor.....	19

This material is reserved for educational use only, not allowed for commercial use.

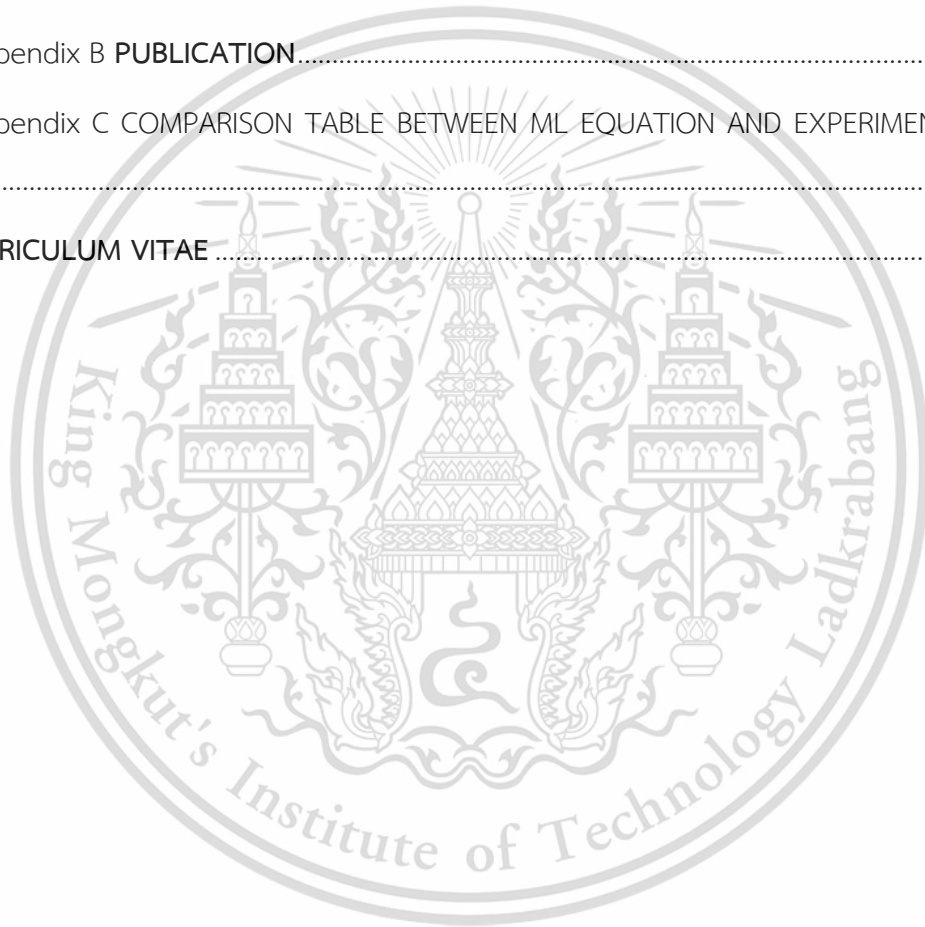
Forbidden to modify the content, and cite the document when use.

3.2.2 Effectiveness of Water-cooling Jacket .....	20
3.2.3 Temperature Fluctuation of Motor .....	22
CHAPTER 4 PART II: VALIDATION.....	24
4.1 RESEARCH METHODOLOGY .....	24
4.1.1 Experimental Setup.....	24
4.1.2 Experimental Conditions.....	24
4.2 RESULTS AND DISCUSSION .....	25
4.2.1 Time Dependent Validation .....	25
4.2.2 Stable State Validation of 3-key Parameters .....	26
4.2.3 Temperature Distribution Validation.....	29
CHAPTER 5 PART III: COMPARISON OF WATER-COOLING JACKETS.....	32
5.1 RESEARCH METHODOLOGY .....	32
5.1.1 Designs for Water-cooling Jackets.....	32
5.1.2 Simulation Setup.....	33
5.1.3 Grid independent technique.....	35
5.1.4 Step-running Technique.....	36
5.1.5 Boundary Condition.....	37
5.2 Results and discussions .....	37
5.2.1 Effect of Flow Rate on Cooling Jacket Model .....	37
5.2.2 Temperature Difference .....	38
5.2.3 Pressure Drop.....	40
5.2.4 Effect of Water Path on Temperature Distribution.....	41
5.2.5 Ranking of Water-cooling Jacket.....	43
CHAPTER 6 PART IV: COOLING STRATEGY .....	44
6.1 RESEARCH METHODOLOGY .....	44
6.1.1 Training Data Collection .....	44
6.1.2 Training Setup .....	45
6.1.3 Vehicle Dynamics in MATLAB/Simulink .....	47
6.1.4 Memory Optimization for Motor Cooling System.....	51
6.1.1 Loss Checking.....	54
6.2 RESULTS AND DISCUSSIONS.....	55
6.2.1 Accuracy of ML Model 1 .....	55

This material is reserved for educational use only, not allowed for commercial use.

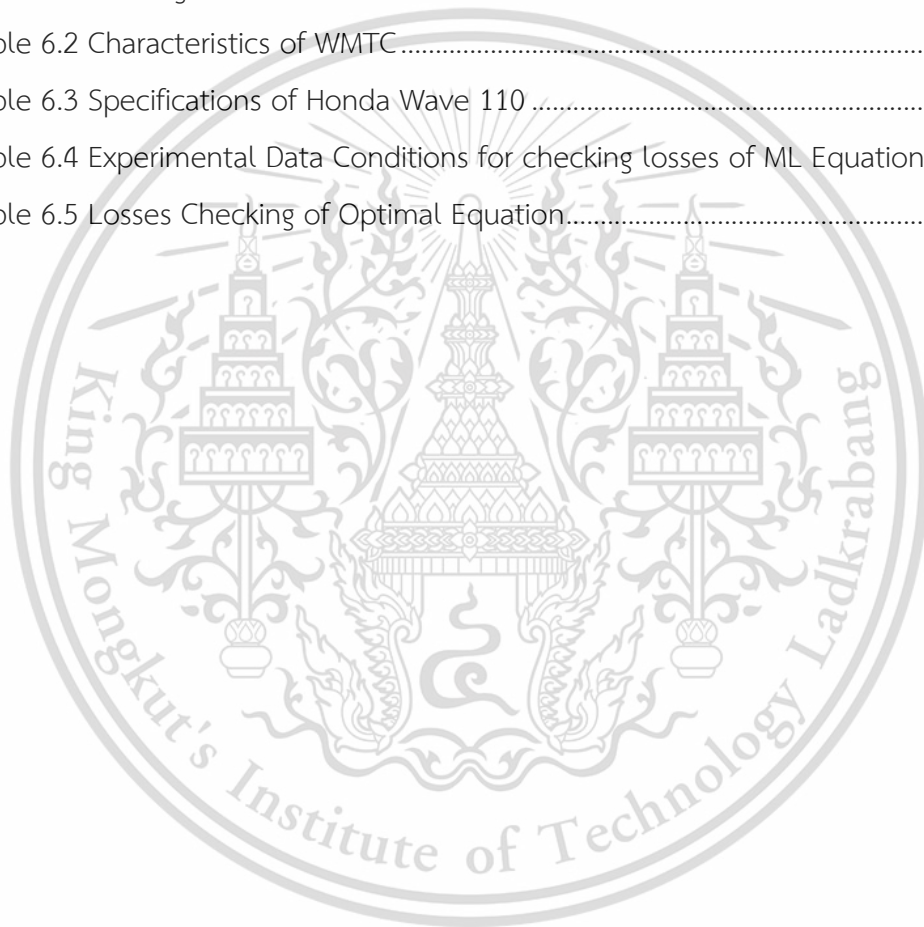
Forbidden to modify the content, and cite the document when use.

6.2.2 Water Utilization.....	56
6.2.3 Optimal ML Equation for Low-memory Processor .....	58
6.2.4 Losses Checking of Optimal Equation .....	59
CHAPTER 7 CONCLUSIONS AND RECOMMENDATIONS .....	61
7.1 CONCLUSIONS .....	61
7.2 DEVELOPMENT DIRECTIONS .....	62
BIBLIOGRAPHY AND REFERENCES .....	63
Appendix A <b>ICOME 2023 CONFERENCE AND CERTIFICATE</b> .....	67
Appendix B <b>PUBLICATION</b> .....	68
Appendix C COMPARISON TABLE BETWEEN ML EQUATION AND EXPERIMENTAL DATA .....	69
CURICULUM VITAE .....	72



## LIST OF TABLES

Table	Page
Table 2.1 Specification of Research Motor.....	6
Table 2.2 Constant Value of Air Resistance Coefficient.....	12
Table 2.3 Rolling Resistance Coefficient according to the road surface condition.....	12
Table 4.1 Experimental Cases.....	25
Table 5.1 Ranking of Water-cooling Jackets.....	43
Table 6.1 Training Cases.....	44
Table 6.2 Characteristics of WMTC.....	50
Table 6.3 Specifications of Honda Wave 110.....	51
Table 6.4 Experimental Data Conditions for checking losses of ML Equation.....	55
Table 6.5 Losses Checking of Optimal Equation.....	59



This material is reserved for educational use only, not allowed for commercial use.

Forbidden to modify the content, and cite the document when use.

# LIST OF FIGURES

Figure	Page
Figure 2.1 Vehicle Dynamic System.....	10
Figure 3.1 Installation of 4 Winding Temperature Sensors.....	16
Figure 3.2 Installation of 4-outer Temperature Sensors.....	16
Figure 3.3 Installation of 3-insulation layers.....	16
Figure 3.4 Setup Schematic of Input Parameter Collection.....	17
Figure 3.5 Sample Result of Inlet and Outlet Temperature. ....	17
Figure 3.6 Sample Result of Motor Heat Generation Calculation.....	18
Figure 3.7 Sample Result of Winding and Jacket Temperature. ....	18
Figure 3.8 Sample Result of AHTC Calculation.....	19
Figure 3.9 Variation of Torque with Different Supplied Currents.....	20
Figure 3.10 Relationship Between Torque and Heat Generation of Motor.....	20
Figure 3.11 Average Winding Time-dependent Temperature.....	21
Figure 3.12 Average Jacket Time-dependent Temperature. ....	21
Figure 3.13 Oscillation of Stator Winding Temperature. ....	22
Figure 3.14 Three-phase Electrical Supply with a Peak Current of 100 A.....	23
Figure 3.15 Three-phase Electrical Supply with a Peak Current of 200 A.....	23
Figure 4.1 Real-time Experimental Setup.....	24
Figure 4.2 Jacket Temperature Comparison Between Simulation and Experiment.....	26
Figure 4.3 Validation of 3 Key parameters at Inlet Temperature of 19.65 °C.....	27
Figure 4.4 Validation of 3-key parameters at Inlet Temperature of 23.5 °C.....	27
Figure 4.5 Validation of 3-key parameters at Inlet Temperature of 27.5 °C.....	28
Figure 4.6 Validation of 3-key parameters at Inlet Temperature of 31 °C.....	28
Figure 4.7 Validation of Four Positions Along Circumference from Inlet to Outlet.....	30
Figure 4.8 Winding Temperature without Cooling.....	31
Figure 5.1 Detailed Topology Comparison of Three Designs.....	32
Figure 5.2 Installation of Water-Cooling Jacket and Motor. ....	34
Figure 5.3 3D-modeling of motor.....	34
Figure 5.4 Exploded View of Motor-water-cooling jacket Combination.....	34
Figure 5.5 Meshing Setup of 3D-modeling.....	36
Figure 5.6 Relationship Between Temperature and Element Numbers.....	36

This material is reserved for educational use only, not allowed for commercial use.

Forbidden to modify the content, and cite the document when use.

Figure 5.7 Step-running of Simulation Process.....	37
Figure 5.8 Effect of Flow Rate on Average Temperature of Motor. ....	38
Figure 5.9 Effect of Flow Rate on Temperature Difference in 3 Models .....	39
Figure 5.10 Effect of Flow Rate on Pressure Drop with Differential Models .....	40
Figure 5.11 Pump Work of Three Different Models as Flow Rate Increases .....	41
Figure 5.12 Temperature Distribution of SWJ.....	42
Figure 5.13 Temperature Distribution of LWJ .....	42
Figure 5.14 Temperature Distribution of MLWJ .....	43
Figure 6.1 Schematic Diagram of Training Process.....	46
Figure 6.2 Decision Tree of Neural Network for Stable State Heat Equation.....	46
Figure 6.3 Block Diagram of Simulink Environment.....	47
Figure 6.4 Power Train System .....	48
Figure 6.5 Applying PID in Controller .....	48
Figure 6.6 Applying ML Model in Controller .....	49
Figure 6.7 World Motorcycle Test Cycle Singal.....	49
Figure 6.8 Simplified Decision Tree of ML model.....	52
Figure 6.9 Simplified Decision Tree of ML Equation.....	52
Figure 6.10 Procedure for Determining the Common Equation.....	53
Figure 6.11 Asymptotic Trending of the Cooling Parameters.....	54
Figure 6.12 Simulink Setup Schematic of Losses Checking.....	55
Figure 6.13 Prediction Accuracy of Motor Temperature .....	56
Figure 6.14 Flow Rate Profile over Time in ML Model Controller.....	57
Figure 6.15 Flow Rate Profile over Time in Logical PID Controller.....	57
Figure 6.16 Calibration Equation between ML Model and Equation .....	59

## LIST OF AND SYMBOLS

$Tq$	Torque of machine
$p$	Number of pole pairs
$U$	Voltage
$U_p$	Internal machine voltage (open circuit voltage)
$\vartheta$	Rotor angle
$\omega_1$	Angular frequency
$X_d$	The main reactance decomposed according to the d-axis
$X_q$	The main reactance decomposed according to the q-axis
$\emptyset$	Motor diameter
$d$	Motor length
$\overline{\Delta T}$	Average temperature difference
$F$	Total tractive force
$R_a$	Aerodynamic resistance
$R_g$	Grade resistance
$R_r$	Rolling resistance of a rear tire
$R_f$	Rolling resistance of a front tire
$R_I$	Inertial resistance
$A$	Contact position between front tire and road surface
$B$	Contact position between rear tire and road surface
$L$	Wheelbase distance
$l_1$	Distance between gravity center and rear wheel contact point
$l_2$	Distance between gravity center and front wheel contact point
$\rho_a$	Density of air
$v$	Flow velocity
$A_v$	The effective cross-sectional area of the vehicle
$c_D$	Constant value of drag coefficient
$P_r$	Ram pressure
$m$	Mass of vehicle
$g$	Acceleration due to gravity
$\alpha$	Slope in degree
$W$	Vehicle weight

This material is reserved for educational use only, not allowed for commercial use.

Forbidden to modify the content, and cite the document when use.

$a$	Linear acceleration
$W_r$	Lift resistance at rear wheel
$W_f$	Lift resistance at front wheel
$Q$	Heat generation of the motor
$F_v$	Flow rate of coolant
$T_{inlet}$	Inlet temperature
$T_{outlet}$	Outlet temperature
$HTC$	Heat transfer coefficient
$AHTC$	Apparent heat transfer coefficient
$\rho_w$	Density of water
$C_p$	Specific heat capacity
$q$	Heat flux
$T_{inside}$	Inside temperature
$T_{outside}$	Outside temperature
$A$	is heat dissipation area
$K_p$	Proportional factor
$K_I$	Integral factor
$K_D$	Derivative factor
$N_u$	Nusselt number
$k$	Thermal conductivity
$L_d$	Characteristic length
$Re$	Reynolds number
$Pr$	Prandtl number
$\mu$	Dynamic viscosity of the fluid

## LIST OF ABBREVIATIONS

EVs	Electric vehicles
ML	Machine learning
ICE	Internal combustion engine
WJ	Water-cooling jacket
SWJ	Short water-path jacket
LWJ	Long water-path jacket
MLWJ	Multi-long water-path jacket
CFD	Computational fluid dynamic
WMTC	World motorcycle test cycle
PID	Proportional-integral-derivative
SynRM	Synchronous Reluctance Motor
MTPA	Maximum torque per ampere
LPM	Litter per minute
Ai	Artificial intelligence
SLPTN	Spatially resolved lumped parameter thermal network
ROM	Reduced order model
PINN	Physics-informed neural network
FEM	Finite element method
AE	Absolute error
RE	Relative error
T1, T2, T3, and T4	4 sensors position at motor winding
T5, T6, T7, and T8	4 sensors position at motor outer
mcTEST	Motor characteristic testbed
Tq1 to Tq10	10 cases of motor torque
IT1 to IT10	10 cases of inlet temperature
FL1 to FL10	10 cases of flow rate
RPM	Round per minute
DNN	Deep neural network
T	Motor temperature and
Ta	The adjusted temperature from calibration

This material is reserved for educational use only, not allowed for commercial use.

Forbidden to modify the content, and cite the document when use.

# CHAPTER 1

## INTRODUCTION

### 1.1 RESEARCH BACKGROUND

When facing the issue of air pollution from internal combustion engines (ICE), such as carbon dioxide, nitrogen dioxide, ozone, particulate matter, and so on, finding an alternative solution is inevitable. In light of this situation, electric vehicles (EVs) have emerged with the aspiration to replace ICE vehicles powered by electric motors (EM) [1]. Despite acknowledging their shortcomings, including electronic waste from microchips, lithium-ion batteries, and electric motors, EVs present a practical solution for the near future. In the current situation, EVs must undergo significant improvements to gain widespread adoption. Among these improvements, EV performance has garnered considerable attention and research efforts [1-4].

One of the crucial factors in enhancing the performance of a motor is temperature control [5]. A motor with an efficient cooling system maximizes its potential more effectively. To fully exploit the cooling system's potential, investigating the factors affecting cooling efficiency is a crucial step. This investigation serves as a basis for analysis and the development of a suitable design tailored to the operating conditions of the motor. Additionally, even with a well-designed system, there's room for improvement to unleash the system's potential fully. Therefore, the next aspect is implementing an intelligent control system to work efficiently.

### 1.2 GOALS AND OBJECTIVES

The main objective of this study is to design a cooling system and optimize its control for a synchronous reluctance motor. To achieve this primary goal, the research needs to address the following sub-objectives:

- To investigate and evaluate the factors influencing the cooling process of a system. The details are presented in Chapter 3.
- To assess the accuracy of the model as well as the simulation process. The specific evaluation is presented in Chapter 4.

- To compare the cooling performance of different designs and provide optimal recommendations for each design. This content is explored in detail in Chapter 5.
- To apply a new control method in the cooling strategy of the system, the method chosen in this study is the application of machine learning (ML) in controlling the flow rate of coolant. An equation of the motor cooling system is derived to optimize memory usage for conveniently interacting with others in a simulation environment. The methodology and detailed results will unfold in Chapter 6.

### 1.3 SCOPE OF WORK

This study selected the synchronous reluctance motor as the subject for constructing the cooling system. Because the characteristics of various motor types can result in differences in methods and cooling systems, the factors influencing the cooling process must be investigated and evaluated to design a rational cooling system. The study directly evaluates these factors through experimentation; in some cases, data not directly collected from experiments undergo simulation. However, all input parameters of the simulation step are collected entirely through the experiment.

Despite input parameters being collected through experimentation, errors in simulation setup procedures can still occur. Therefore, this study conducted a comprehensive validation step to compare simulation results with experiments in three aspects:

- Validation of temperature variation over time.
- Validation was performed under 64 different conditions in a stable state, involving three key parameters: the heat generation of the motor, the flow rate of the coolant, and the inlet temperature. The heat generation of the motor was controlled through the supplied current during the experiments.
- Validation of temperature distribution at various motor positions based on the installation of sensors around the motor circumference.

The topology of the water-cooling jacket (WJ) also significantly impacts cooling performance. Three different designs, named short water-path jackets (SWJ), long

This material is reserved for educational use only, not allowed for commercial use.

water-path jackets (LWJ), and multi-long water-path jackets (MLWJ), were evaluated under the same boundary conditions. Computational fluid dynamics (CFD) methods were employed to assess these designs' differences in temperature difference, pressure drop, and temperature distribution.

A well-designed system can lose its effectiveness if the control strategy is inadequate. This study integrates design and control aspects to leverage the potential of a cooling system fully. Machine learning (ML) is employed as an optimal control method for the system. The research presents the training outcomes of the ML model and assesses the efficacy of this approach when applied to the vehicle powertrain in the MATLAB/Simulink environment. The world motorcycle test cycle (WMTC) serves as the testing signal in the Simulink diagram. To evaluate ML efficiency, comparing the ML method and the proportional-integral-derivative (PID) control method was implemented. This study ends by finding an equation from the motor cooling system box to interact with another system conveniently.

#### **1.4 OUTLINE OF THESIS**

This study comprises 7 chapters. The current chapter presents an introduction, including the research background, goals and objectives, work scope, and thesis outline.

Chapter 2 provides the theoretical foundations and background knowledge necessary to build upon for the research in the following chapters.

Chapter 3 serves as the preliminary study, presenting surveys and evaluations of factors influencing the cooling process. Additionally, this chapter outlines the process of collecting input parameters for subsequent simulation steps.

Chapter 4 introduces a comprehensive validation method for the study. This section verifies the accuracy of the simulation results, ensuring a more reliable basis for subsequent research.

Chapter 5 presents the process and results of comparing various cooling designs and evaluating the effect of their topologies on the other cooling parameters.

Chapter 6 presents the ML model's training process, which is employed in the cooling strategy, and evaluates its control effectiveness compared to the PID method

in the MATLAB/Simulink environment. An ML equation derived from the motor cooling system box is also presented.

Chapter 7 entirely summarizes the results obtained in the thesis and provides a comprehensive conclusion along with directions for possible future research.



This material is reserved for educational use only, not allowed for commercial use.

Forbidden to modify the content, and cite the document when use.

## CHAPTER 2

### LITERATURE REVIEW

#### 2.1 SYNCHRONOUS RELUCTANCE MACHINE

The synchronous reluctance motor (SynRM) includes non-permanent magnetic poles on the ferromagnetic rotor and does not have windings on the rotor. This implies that SynRM generates reluctance torque from changing magnetic reluctance, also known as magnetic resistance. Because the flux tends to flow towards the lowest resistance, once generated by the stator, the flux will flow towards the lowest resistance within the rotor [6]. This causes the rotor torque to rotate in the direction of minimum resistance. Therefore, the load capability of SynRM is highly regarded, especially at low speeds [7].

The torque of the salient-pole synchronous machine consists of two components: one generated by the excitation current and the other produced by the differing reluctance in the d- and q-axes, as expressed by Equation (2.1) [8].

$$Tq = \frac{3p}{\omega_1} \left( \frac{U \cdot U_p}{X_d} \sin(\vartheta) + \frac{U^2}{2} \left( \frac{1}{X_q} - \frac{1}{X_d} \right) \sin(2\vartheta) \right) \quad (2.1)$$

where  $Tq$  is torque of machine,  $p$  is number of pole pairs,  $U$  is voltage,  $U_p$  is internal machine voltage (open circuit voltage),  $\vartheta$  is rotor angle,  $\omega_1$  is angular frequency,  $X_d$  and  $X_q$  are the main reactance decomposed according to the d-axis and q-axis, respectively.

If torque due to the difference in reluctance is considered alone, while excitation winding, slip rings, and brushes are disregarded, the torque is calculated according to Equation (2.2).

$$Tq = \frac{3p}{\omega_1} \cdot \frac{U^2}{2} \left( \frac{1}{X_q} - \frac{1}{X_d} \right) \cdot \sin(2\vartheta) \quad (2.2)$$

In this study, the SynRM is used as the tractive motor for the motorcycle, with detailed specifications provided in Table 2.1. The maximum torque per ampere (MTPA) approach is employed to measure the maximum motor torque based on the supplied current [9]. During experimentation, a stable load state is maintained by providing

This material is reserved for educational use only, not allowed for commercial use.

Forbidden to modify the content, and cite the document when use.

current to the stator. Since the majority of flux is generated from the stator, this motor type is highly suitable for WJ installed around the motor.

**Table 2.1 Specification of Research Motor**

Motor rated power	3 kW
Type of motor	Synchronous reluctance motor
DC supply voltage	72 VDC
Motor nominal speed	5,000 rpm
Motor maximum speed	8,000 rpm
Motor nominal torque	5.7 Nm (3 kW)
Motor maximum torque	9.5 Nm (5 kW)
Max. efficiency	90 %
Max. stator current density	15 A/mm <sup>2</sup>
Max. flux density in stator teeth	1.6 T
Motor cooling type	Totally enclosed
Motor operating temperature	130 C
Motor dimension ( $\varnothing, d$ )	140 mm

## 2.2 TYPES OF COOLING METHOD

SynRM incorporates temporary magnetic poles within the ferromagnetic rotor, with the winding absent on the rotor itself. This suggests that its torque is solely produced through magnetic reluctance. The increasing temperature within the stator winding also affects the torque density and energy consumption [10]. Therefore, managing the temperature of the motor is essential to overcome if one wishes to enhance motor torque and EV performance.

One of the oldest cooling methods for motors is the thermal sink, with heat sink fins surrounding the motor to dissipate heat into the environment [11, 12]. However, to meet the high torque demands in usage scenarios such as transportation vehicles, this method is gradually becoming less suitable. For operating transportation vehicles, the torque of the vehicle constantly varies depending on driving habits and road conditions, so the cooling system needs to be proactive and flexible in different situations. Therefore, alternative cooling methods are being explored.

This material is reserved for educational use only, not allowed for commercial use.

Forbidden to modify the content, and cite the document when use.

Even though thermal sink is no longer suitable, air cooling can still be applied to cool the motor because its oxidation rate is much lower than that of liquid cooling. Hongmin Li [13] designed a cooling fan attached to the electric motor shaft, and a computer fluid dynamics (CFD) model was developed, with airflow velocity measured through experiments. A comparison between the model and experiments showed quite good agreement. The research results indicate that the airflow velocity for cooling is proportional to the rotational speed of the motor, while the motor speed is inversely proportional to the external load level. This sets a cooling limit for this design, as the load increases, the heat generation of the motor increases, requiring the cooling system to operate more actively. To improve cooling efficiency, Shuye Ding et al. [14] combined a thermal sink with a fan attached to the rotor of the motor. This research provided specific calculations regarding the relationship between air friction losses and fan characteristics. The study results demonstrated the effectiveness of combining end winding with a self-supporting fan. The maximum temperature decreased from 124.45 K to 95.69 K, representing a reduction of 28.76 K (23.11%). Although this combined design yields significant benefits, it still depends on the speed of the rotor and shares common limitations with Hongmin Li's research. To ensure that the fan speed is not dependent on the speed of the rotor, Chiwon Kim et al. [15] used an external fan with a constant flow rate of 0.2 m<sup>3</sup>/s. This fan, an air-gap fan, positioned on the rotor, utilizes air convection to direct airflow into the motor through six inlets on the left side of the frame. The results showed a 55% improvement in cooling efficiency in the 24,000 to 30,000 rpm range when using two air-gap fans, one positioned in front and one in the rear. For a single fan positioned at the rear, there was a 36% improvement in cooling efficiency, indicating that rear placement is more effective than front placement. However, air cooling is limited by its low capacity and thermal conductivity, which are lower compared to oil cooling and liquid cooling [16].

Federico Marcolini et al. [17] proposed a novel direct oil cooling system. This cooling design allows the liquid to flow directly through the end portion of the motor coil. The simulation results were validated through experiments, showing that direct oil cooling makes it possible to remove up to 2.87 times more heat compared to indirect water cooling. However, this comparison seems somewhat unfair between the two cooling methods. In a study conducted by Pia Lindh et al. [18], the comparison

was made among indirect water cooling, direct liquid cooling-oil, and direct liquid cooling-water, with maximum temperatures of 137 °C, 86 °C, and 57 °C, respectively. Hence, under equivalent direct cooling conditions, water cooling is more effective than oil cooling. This can be explained by the higher thermal conductivity of water compared to oil.

Additionally, promising concepts related to hydric cooling have garnered considerable research interest. Borja Prieto et al. [19] introduced the idea of integrating air and water cooling. The standout feature of this concept is a closed-loop cooling system. A water-cooling jacket (WJ) is employed to cool the outer part of the motor, while inside the motor, cooling is conducted by a fan inserted on the rotor, with the hot air subsequently cooled by the water-cooling jacket as well. This idea is incredibly brilliant. In densely populated urban areas where traffic jams are common, the air often doesn't have the chance to flow into the motor compartment for cooling. However, as stated in the aforementioned studies [13, 14], the speed of cooling fan depends on the rotor speed, which constrains the effectiveness of air cooling. It would be perfect ideal to have a control system to optimize the flow rate of the WJ. Unfortunately, this research maintained the flow rate at 75 LPM. Another hydric cooling method was proposed by Bishal Silwal et al. [20], which combines the water-cooling jacket (WJ) with direct oil cooling. This study also provides a comparative evaluation between solely using the water-cooling jacket and combining the water-cooling jacket with direct oil cooling. The results show that the hydric method significantly improves efficiency.

The hydric methods presented above are indeed fantastic ideas. However, they require significant modifications to the original motor design. Similarly, direct oil cooling poses similar challenges. Modifying the design will alter the initial material calculations of the motor, potentially compromising the material integrity during operation. In the case of air cooling, thermal sinks are efficiency is low and cooling fans are limited by the rotational speed of the rotor. For these reasons, the water-cooling jacket emerges as the most suitable candidate, as it doesn't require modifications to the original design. The water-cooling jacket only serves as an additional component, easily installable into the motor. With higher thermal conductivity compared to oil and air, water is a suitable coolant for indirect cooling methods. Even with a well-designed cooling

system, its effectiveness diminishes without a good control system. This study aims to comprehensively balance design and control to maximize its potential.

### 2.3 ADVANTAGE OF MACHINE LEARNING

Thanks to the environmental friendliness and the growing recognition of EV applicability in daily life, along with advancements in science and technology, artificial intelligence (AI) is increasingly being utilized across various aspects of EVs. These include energy management [21], predicting remaining EV miles [22], motor diagnostics [23], and more.

The application of machine learning in safety aspects of motors, such as cooling systems, is garnering increasing interest from researchers and yielding significant achievements over time. Henning Sauerland et al. [24] have provided a comparison of four methods for estimating the temperature of electric motors. Specifically, the study compared the spatially resolved lumped parameter thermal network (SLPTN), reduced order model (ROM), machine learning (ML) model, and physics-informed neural network model (PINN) on electric machine using a direct oil-cooling system. In the study, an assessment was provided concerning the ML model, indicating it as a method with high accuracy and easy setup. However, since this approach relies on large datasets, big data, its accuracy may decrease due to unawareness. The accurate deployment of the model necessitates a large volume of data. Also, in their study on predicting electric motor temperatures, Wilhelm Kirchgässner et al. [25] concluded that good efficiency can be achieved with approximately 60 hours of recorded data. This demonstrates the feasibility of applying machine learning to cooling systems.

In another application within cooling systems, Yuncong Wang et al. [26] computed the topology of the water path under various operating conditions to identify the structure with the best efficiency. After data collection and processing, 20% of the data is reserved for the test set, and 80% is used for the training set. The higher the R-value, approaching 1, indicates a model with high accuracy and reliability. Additionally, this design stands out for its innovative approach of utilizing machine learning to assess the design. This combination is highly intriguing and lays the groundwork for further exploration in future applications. M. Weber et al. [27] also explore another interesting combination: using machine learning alongside finite

element method (FEM). To simplify the FEM model, ML algorithms are used to model the input-output relationships. The results indicate that the most accurate network consists of 2 hidden layers with 4 and 8 neurons, respectively. The average accuracy of predictions in the thermal neural network model is  $\overline{\Delta T} = -0.15 \pm 1.36$  °C.

However, these studies only employ machine learning for assembling data, modeling input-output relationships, and stop at design calculation and evaluation. ML models stand out for their ability to make optimal decisions under various conditions. It would be very useful to apply them to control cooling systems.

## 2.4 VEHICLE DYNAMICS

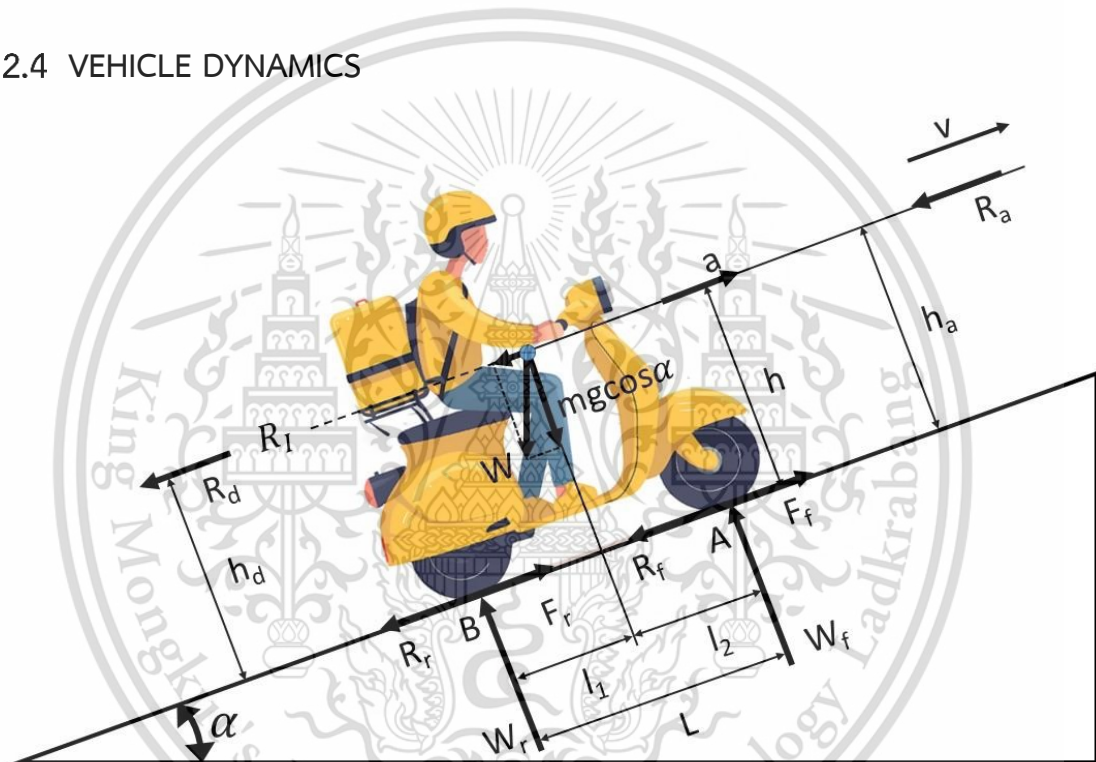


Figure 2.1 Vehicle Dynamic System

Leveraging existing laboratory equipment, this research is conducted on motor of motorcycle. The results will demonstrate the accuracy of the research methodology and its feasibility when applied to higher-powered motors. Vehicle dynamics can be modeled in the Matlab/Simulink environment using mathematical formulas while the vehicle is in motion, with illustrated images presented in Figure 2.1 [28].

When considering a one-axle vehicle and applying Newton's first law, the equations along the longitudinal axis (x) are presented as Equation (2.3) [29, 30].

$$F = R_a + R_g + R_r + R_l \quad (2.3)$$

The required tractive force is evaluated by summing the components of resistance. Where  $F$  is total tractive force,  $R_a$  is aerodynamic resistance,  $R_g$  is grade resistance,  $R_r$  is rolling resistance of a rear tire, and  $R_I$  is inertial resistance.

### 2.4.1 Aerodynamic Resistance

At average or higher velocities of the vehicle, aerodynamic resistance and torque not only affect the vehicle performance and power consumption but also influence its dynamic behavior. The basic aerodynamic resistance is divided into three main physical effects:

- The form resistance is generated by the turbulent motion of the airflow behind the vehicle, and this effect accounts for approximately 85 % of the total aerodynamic resistance.
- The friction resistance is generated by the shear flow on the chassis and depends on its surface area. This effect accounts for approximately 10 % of the total aerodynamic resistance.
- The inner resistance, in reality, is caused by one part of the airflow passing through the chassis. This portion of air serves to cool the motor and ventilate the passenger space. This effect accounts for approximately 5% of the total aerodynamic resistance.

The majority of the wind force is caused by turbulent streams and is proportional to the ram pressure, as depicted in Equation (2.4).

$$P_r = \frac{1}{2} \cdot \rho_a \cdot v^2 \quad (2.4)$$

where  $\rho_a$  is density of air,  $v$  is flow velocity. With ram pressure, along with the effective cross-sectional area  $A_v$  of the vehicle and a constant value of drag coefficient  $c_D$ , we can calculate aerodynamic resistance  $R_a$  using Equation (2.5). Table 2.2 presents the reference constant values for various types of vehicles. Since the focus of this study is motorcycles, a coefficient of 0.6 is chosen for air resistance calculations.

$$R_a = P_r \cdot A_v \cdot c_D \quad (2.5)$$

Table 2.2 Constant Value of Air Resistance Coefficient

Vehicle type	Wind resistance $C_D$
Passenger vehicle	0.2-0.4
Truck	0.6-1.0
Bus	0.6-0.7
Motorcycle	0.6

### 2.4.2 Grade Resistance

This resistance force occurs when the vehicle is going uphill or downhill. Essentially, it is the gravitational component of the vehicle divided when it is on an incline. This force has a direction along the slope of the incline and is represented by Equation (2.10).

$$R_g = m \cdot g \cdot \sin(\alpha) \quad (2.6)$$

where  $m$  is mass of vehicle,  $g$  is acceleration due to gravity, and  $\alpha$  is slope in degree.

### 2.4.3 Rolling Resistance

At low speeds, rolling resistance stands as the primary force impeding the motion of a vehicle. While other resistive forces affect certain motion conditions, rolling resistance comes into play from the moment the vehicle begins to roll. Moreover, a considerable portion of the energy expended during the rolling motion of the vehicle is transformed into heat within the tire, significantly impacting the properties and performance of both the tire and its constituent materials. Rolling resistance is calculated based on Equation (2.7), with  $C_r$  is rolling resistance coefficient, referenced from Table 2.3.

Table 2.3 Rolling Resistance Coefficient according to the road surface condition

Road surface condition	Value of rolling resistance coefficient
Concrete or Asphalt	0.013
Gravel	0.02
Macadam	0.025
Soil	0.1-0.35

This material is reserved for educational use only, not allowed for commercial use.

Forbidden to modify the content, and cite the document when use.

$$R_r = m \cdot g \cdot c_r \cdot \cos(\alpha) \quad (2.7)$$

#### 2.4.4 Inertial resistance

Newton's second law of motion states that the vector sum of the forces acting on an object is equal to the mass of that object multiplied by its acceleration. Mathematically, it is expressed as Equation (2.8), where  $R_I$  represents the inertial resistance,  $W$  is vehicle weight, and  $a$  is linear acceleration. This law describes how the acceleration of a vehicle is directly proportional to the net force acting on it and inversely proportional to its mass. It also specifies that the acceleration always occurs in the direction of the applied force.

$$R_I = \frac{W}{g} \cdot a \quad (2.8)$$

#### 2.4.5 Lift Force

This force generated at the point where the tires contact the road surface. It is the counterforce created by a portion of the vehicle weight, as presented in Equation (2.9). When the vehicle ascends a slope, its weight is divided into lift force and rolling resistance. When the vehicle is traveling on a flat road, the lift force is equal to the weight of the vehicle.

$$W_r + W_f = m \cdot g \cdot \cos(\alpha) \quad (2.9)$$

where  $W_r$  is lift resistance at rear wheel and  $W_f$  is lift resistance at front wheel.

### 2.5 ABSOLUTE AND RELATIVE ERROR

Absolute or relative error is often used to determine the difference between the values obtained from the experiment and those from the simulation.

- Absolute Error (AE): This is the absolute value of the difference between the experimental and simulated values. It gives magnitude of the discrepancy without considering direction.

$$AE = |\textit{Experimental Value} - \textit{Simulated Value}| \quad (2.10)$$

- Relative Error (RE): This error is expressed as a percentage of the experimental value.

$$RE (\%) = (AE / \textit{Experimental Value}) \cdot 100\% \quad (2.11)$$

By comparing these errors, the accuracy of the simulation results relative to the experimental data can be assessed. Lower errors indicate better agreement between the simulation and experimental results.



## CHAPTER 3

### PART 1: EFFECT OF FACTORS ON COOLING PROCESS

#### 3.1 COLLECTING INPUT PARAMETERS

In this chapter, factors affecting efficiency were surveyed and evaluated. To make the simulation process more realistic, the input parameters were collected through experiments. These include heat generation of the motor ( $Q$ ), flow rate ( $F_v$ ), inlet temperature ( $T_{Inlet}$ ), and apparent heat transfer coefficient ( $AHTC$ ). While flow rate and inlet temperature can be collected using a volume flow rate meter and temperature sensor, heat generation of the motor and apparent heat transfer coefficient cannot be directly collected like the other two parameters and must be obtained through equations (3.1) and (3.2).

$$Q = F_v \cdot \rho_w \cdot C_p \cdot (T_{outlet} - T_{inlet}) \quad (3.1)$$

$$AHTC = \frac{q}{T_{inside} - T_{outside}} \quad (3.2)$$

$$q = \frac{Q}{A} \quad (3.3)$$

where  $\rho_w$  is density of water [ $kg/m^3$ ],  $C_p$  is specific heat capacity [ $J/kg \cdot K$ ],  $T_{outlet}$  is outlet temperature [ $^{\circ}C$ ],  $q$  is heat flux [ $w/m^2$ ],  $T_{inside}$  is inside temperature,  $T_{outside}$  is outside temperature, and  $A$  is heat dissipation area [ $m^2$ ].

To gather comprehensive data on the cooling process, temperature sensors are arranged with four sensors inside the motor winding and four sensors on the outer surface of the motor, labeled as T1, T2, T3, and T4 for the internal sensors and T5, T6, T7, and T8 for the external sensors, as indicated in Figure 3.1 and Figure 3.2. These positions were strategically located along the water channel's circulation path of SWJ. The temperature distribution was expected to increase gradually from T1 to T4 and from T5 to T8. This arrangement also served as part of the validation process in the subsequent chapter. The exterior of the jacket was enveloped by three layers of

This material is reserved for educational use only, not allowed for commercial use.

insulation, as depicted in Figure 3.3. These insulation layers serve the purpose of isolating the motor from the external air, ensuring that heat transfer occurs only from the motor to the cooling water. This plays a crucial role in determining the apparent heat transfer coefficient (AHTC).

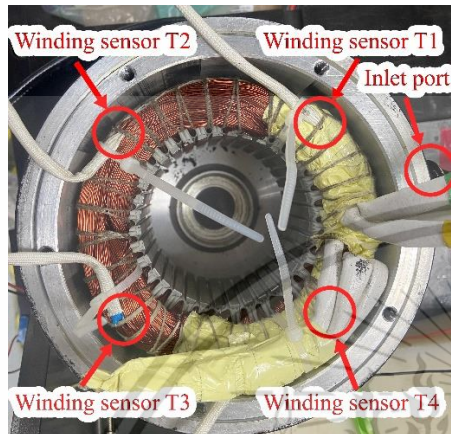


Figure 3.1 Installation of 4 Winding Temperature Sensors.

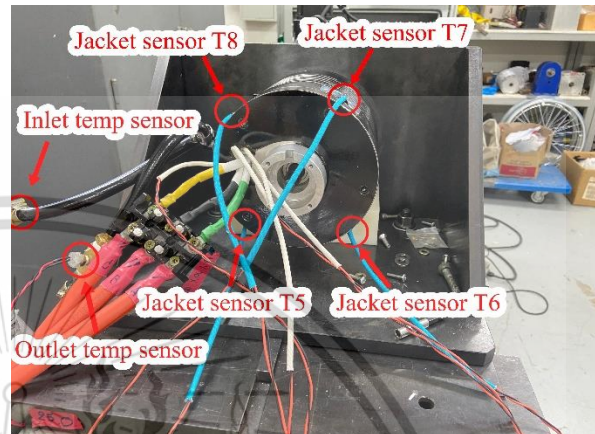


Figure 3.2 Installation of 4-outer Temperature Sensors.

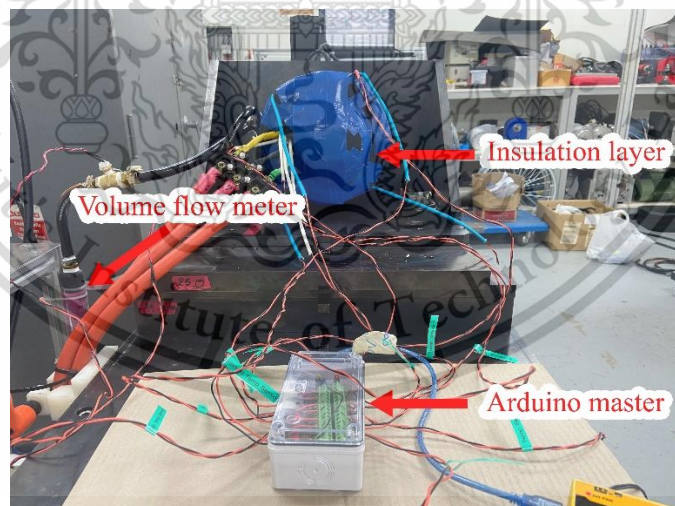


Figure 3.3 Installation of 3-insulation layers.

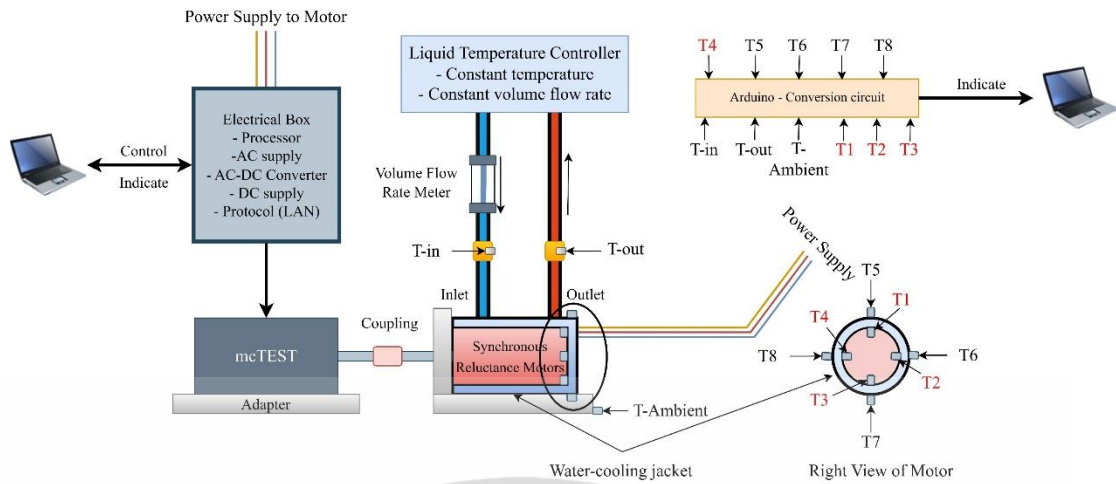


Figure 3.4 Setup Schematic of Input Parameter Collection.

Based on Equation (1), the method for collecting heat generation of the motor has been arranged as depicted in Figure 3.4, with a volume flow rate meter, inlet temperature sensor, and outlet temperature sensor installed. Temperature data collected from the sensors will be processed by the Arduino master and displayed by the LabVIEW platform. The data transfer process from Arduino to LabVIEW is executed through the serial port.

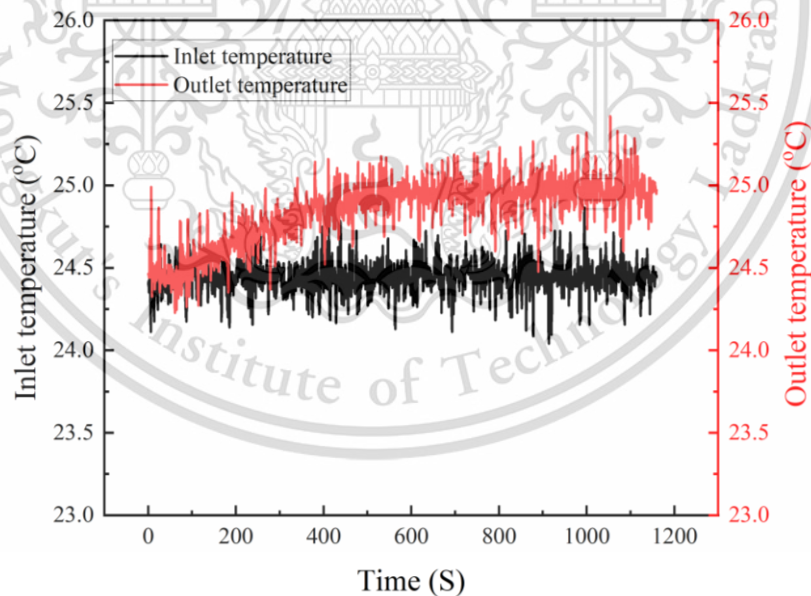
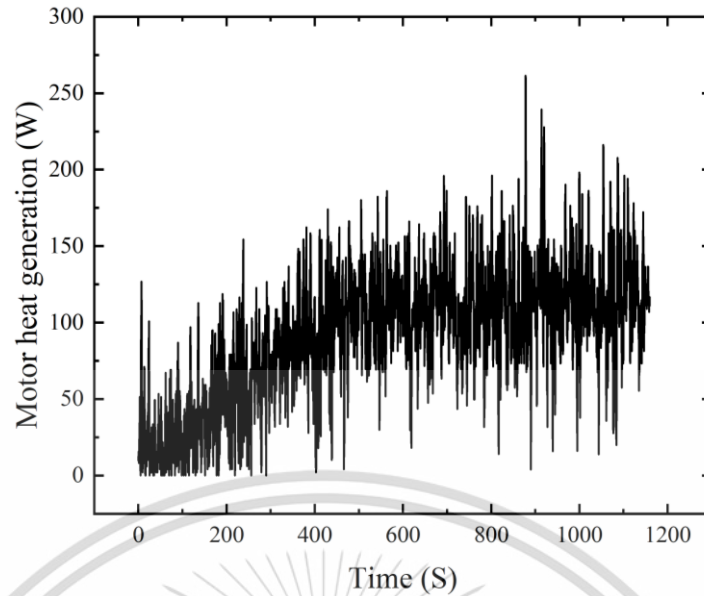
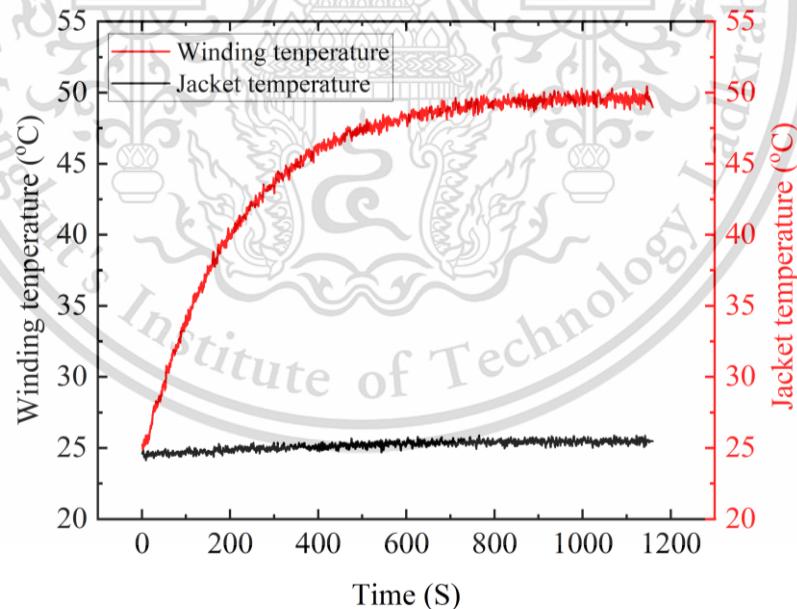


Figure 3.5 Sample Result of Inlet and Outlet Temperature.



**Figure 3.6 Sample Result of Motor Heat Generation Calculation.**

The sample experiment results are represented in Figure 3.5, showing the inlet and outlet temperatures. These results were collected under the condition of a peak current of 200 A, an inlet temperature of 24.45°C, and a flow rate of 2.25 LPM. After applying Equation (3.1), the heat generation of the motor is calculated as shown in Figure 3.6. This will serve as the input parameter used for simulation.



**Figure 3.7 Sample Result of Winding and Jacket Temperature.**

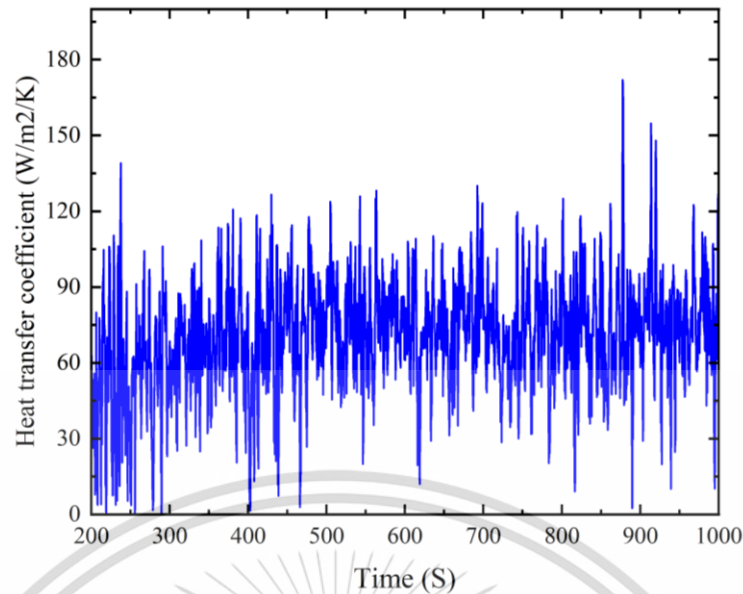


**Figure 3.8 Sample Result of AHTC Calculation.**

Following the same concept and boundary conditions, the sampled results of inside temperature and outside temperature are depicted in Figure 3.7. After applying Equations (3.2) and (3.3), AHTC is calculated as shown in Figure 3.8. This is a crucial parameter for explaining the differences in distribution in the subsequent chapters.

## 3.2 RESULTS AND DISCUSSION

### 3.2.1 Torque and Heat Generation of Motor

As outlined in Figure 6.3, the input signal of the powertrain system is WMTC. Consequently, after computing through the various resistance moments, the ML model input must be torque. Figure 3.9 presents the result of determining the maximum torque of the motor based on the maximum supplied current and illustrates the torque change with the rotor rotation angle, referred to as the grammar angle.

The maximum torque for 100 A, 135 A, 170 A, and 200 A is 1.76 Nm, 3.08 Nm, 4.39 Nm, and 5.46 Nm, respectively. These results also serve as the intermediate conversion step for Table 4.1 and Table 6.4.

When the supply current increases, the heat inside the motor windings also rises accordingly. This illustrates the relationship between torque and heat generation in the motor, as shown in Figure 3.10, and explains the necessity of effective cooling when the vehicle operates in harsh environments and requires high torque.

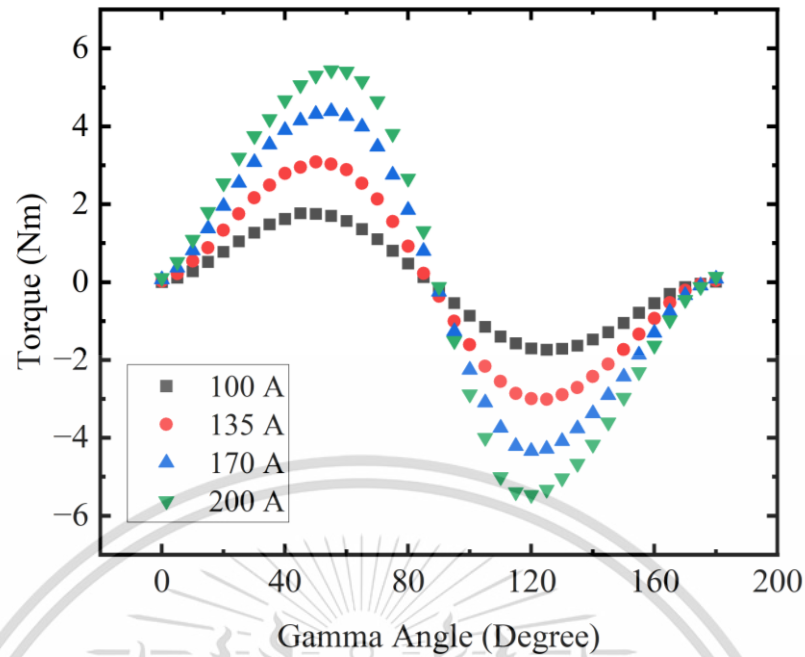


Figure 3.9 Variation of Torque with Different Supplied Currents

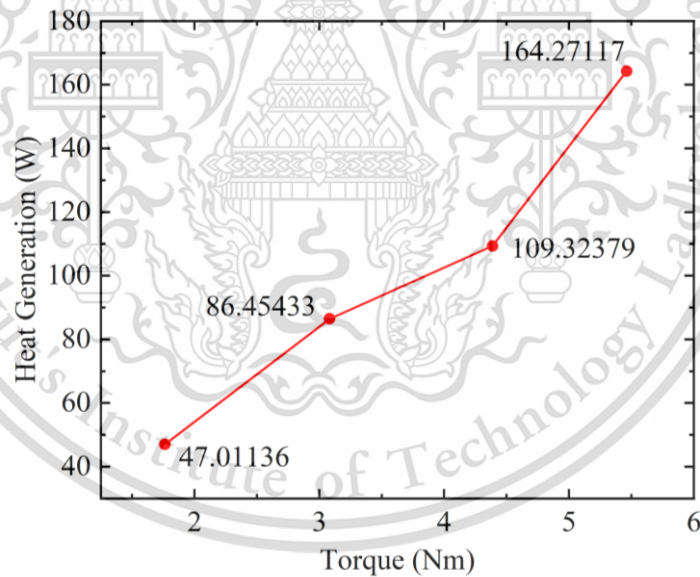


Figure 3.10 Relationship Between Torque and Heat Generation of Motor

### 3.2.2 Effectiveness of Water-cooling Jacket

In Figure 3.11 and Figure 3.12, the experimental results have demonstrated the effective thermal behaviour of the motor after combining with the WJ. With a supplied current of 200 A, as the flow rate increased from 0 LPM to 2.25 LPM and then to 3.2 LPM, the stator winding temperature and jacket cover temperature significantly

dropped from 70.20 °C to 51.71 °C and further to 50.45 °C, and from 42.23 °C to 26.14 °C and then to 25.89 °C, respectively.

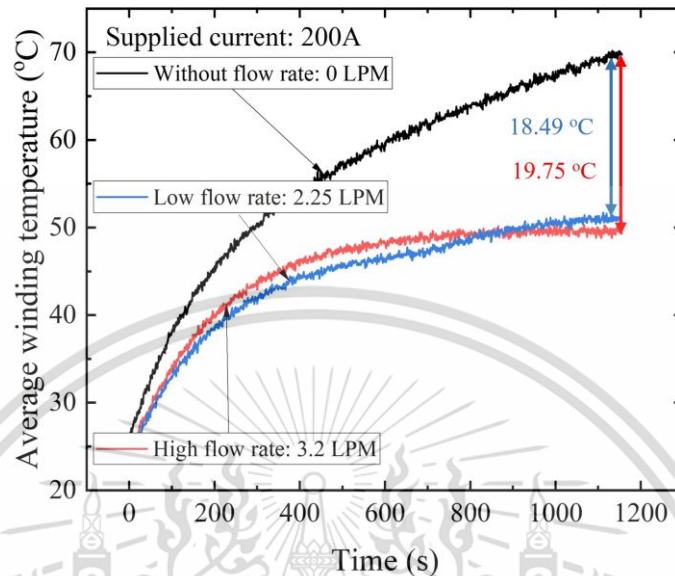


Figure 3.11 Average Winding Time-dependent Temperature.

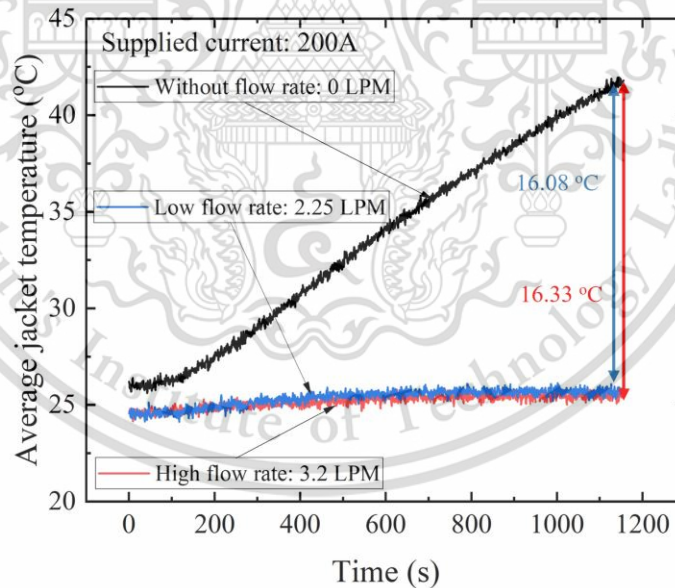
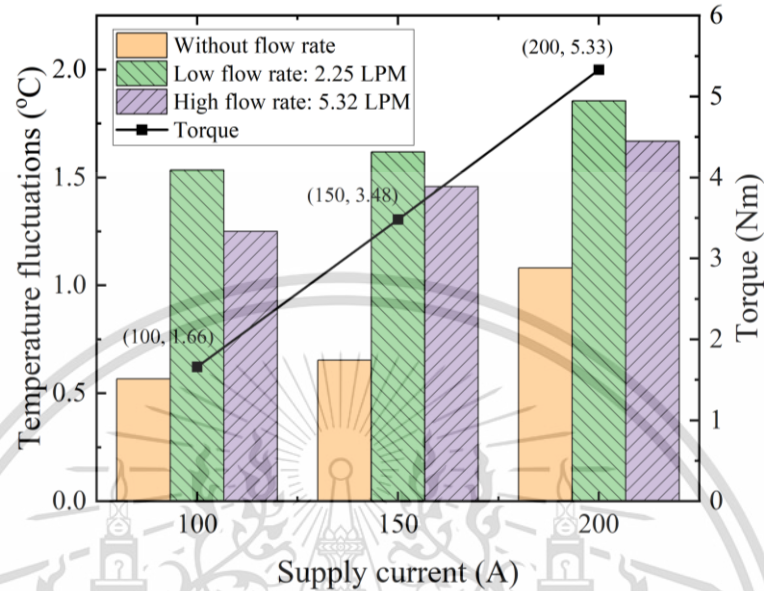


Figure 3.12 Average Jacket Time-dependent Temperature.

Temperatures at position T5, T6, T7, and T8 were 24.91 °C, 25.78 °C, 26 °C, and 26.03 °C, respectively. It was observed that the temperature gradually increases from the inlet to the outlet due to the circular topology of the SWJ. Despite conducting experiments at three different volume flow rates, the heat generation of the motor remains approximately consistent at 100 A, 150 A, and 200 A, calculating 30 W, 65 W, This material is reserved for educational use only, not allowed for commercial use.

and 110 W, respectively. Therefore, the computed experimental results can be confidently employed as input parameters for the simulation process.

### 3.2.3 Temperature Fluctuation of Motor



**Figure 3.13 Oscillation of Stator Winding Temperature.**

Figure 3.11 and Figure 3.12 reveal fluctuations in both the stator winding and jacket temperatures. Xiaofeng Yang's study similarly appeared this phenomenon and explained with thermocouple implementations [31]. However, Figure 3.13 demonstrated that temperature fluctuations were impacted by the supplied current and flow rate.

Remarkably, the lowest temperature fluctuations consistently occur when there was no flow rate. As the supplied current increases, the temperature oscillations also rise. Specifically, the supplied currents of 100 A, 150 A, and 200 A, the temperature fluctuations without flow rate were approximately 0.57 °C, 0.65 °C, and 1.08 °C, respectively. This can be explained by the increasing current oscillation of the three-phase current. Specifically, for a peak current of 100 A, the current phase shift oscillates with a magnitude of 50 A, as shown in Figure 3.14. When the peak current increases to 200 A, the current phase shift oscillation also increases, reaching up to 100 A, as depicted in Figure 3.15.

Conversely, with an elevation in the flow rate, temperature oscillations diminish. For instance, at a current level of 200 A, as the flow rate rose from 2.25 LPM to 5.32 LPM, the temperature fluctuation declined from 1.86 °C to 1.67 °C. This

outcome resonates with the findings in Shigeki Hirasawa's research, attributing this trend to the augmentation in the volume of water flow [32].

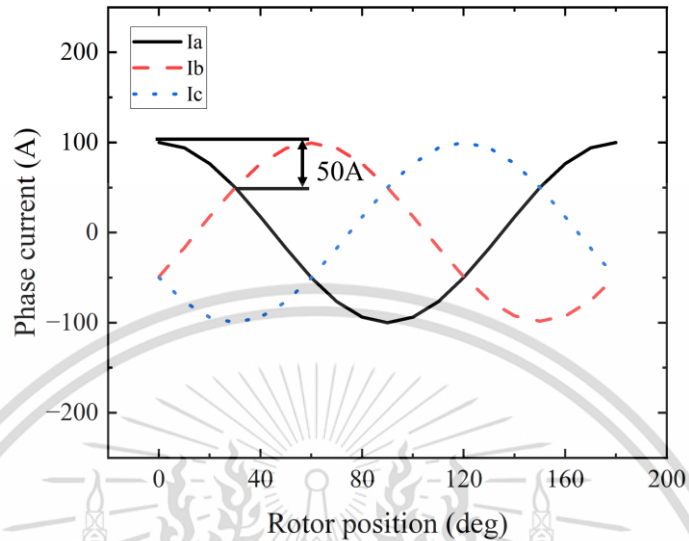


Figure 3.14 Three-phase Electrical Supply with a Peak Current of 100 A

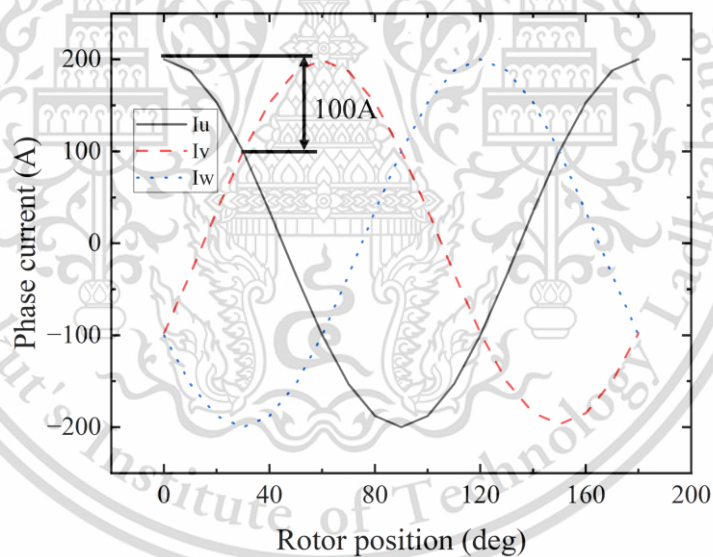


Figure 3.15 Three-phase Electrical Supply with a Peak Current of 200 A

Research conducted by I. Y. Braslavsky concluded that temperature oscillations expedite the aging process of the stator winding insulation [33]. This presents a subsequent challenge when aiming to improve motor torque following a reduction in its maximum temperature.

## CHAPTER 4

### PART II: VALIDATION

#### 4.1 RESEARCH METHODOLOGY

##### 4.1.1 Experimental Setup

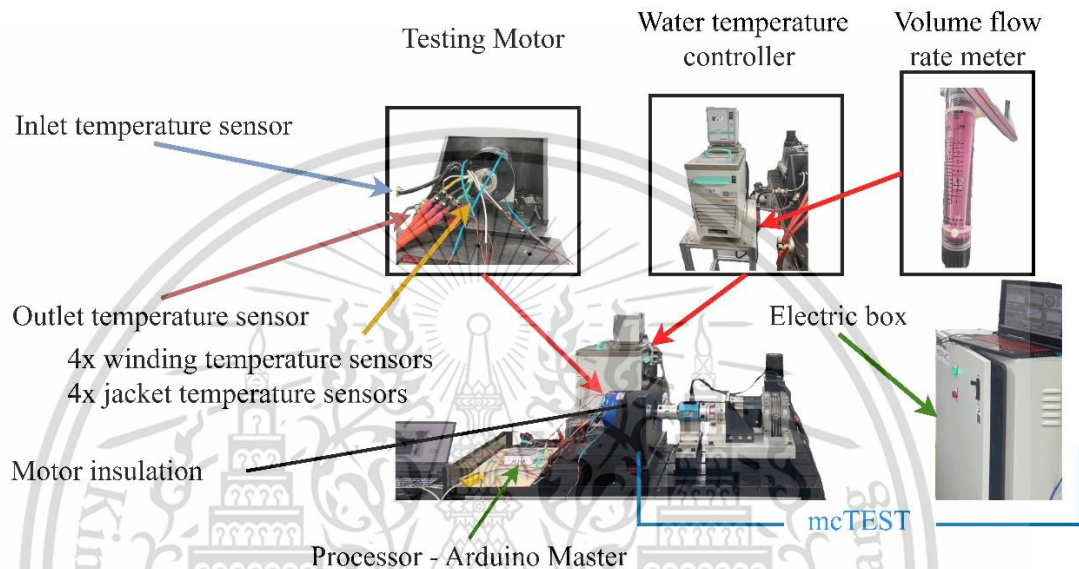


Figure 4.1 Real-time Experimental Setup.

Despite input parameters being collected through the experimental process, model inaccuracies can still occur. Therefore, simulation results require validation to ensure confidence in their accuracy and reliability. Validation of the results is a necessary step. In this study, validation is performed through testing, and its setup is described in Figure 4.1. This setup consists of a motor characteristic testbed (mcTEST) [9], a synchronous reluctance motor (SynRM) equipped with a water-cooling jacket, and a water temperature controller. The mcTEST is a static testing system that utilizes the MTPA approach. During testing, heat generation of the motor is produced corresponding to different torque levels of the motor. Consequently, the cooling process was applied for experimentation and evaluation.

##### 4.1.2 Experimental Conditions

There are numerous factors influencing the cooling performance of the motor, such as ambient temperature, torque of the motor, flow rate of coolant, inlet temperature, and design of the cooling system. Among these, ambient condition is an objective and stable factor and can be considered constant, the motor design remains

This material is reserved for educational use only, not allowed for commercial use.

Forbidden to modify the content, and cite the document when use.

fixed after manufacturing. The torque of the motor, flow rate of coolant, and inlet temperature are factors capable of being controlled and adjusted during the cooling process. As mentioned in Figure 5.8, to balance pump capacity and cooling efficiency, the flow rate of coolant should not exceed 3 LPM. The experimental conditions are also constrained by this limit of 3 LPM. Additionally, Table 2.1 illustrates that the maximum torque of the motor is 9.5 Nm. Moreover, these experimental conditions are set to validate the cooling model designed and controlled to operate in Southeast Asian countries, specifically in Thailand, so the inlet temperature is specified to range from 19.65 °C to 31 °C, covering locations from Chiang Mai to Bangkok. The specific experimental conditions are outlined in Table 4.1.

**Table 4.1 Experimental Cases**

No	Supplied Current (A)	Inlet Temperature (°C)	Flow Rate (LPM)
1	100	19.65	1.9
2	135	23.5	2.25
3	170	27.5	2.5
4	200	31	3

## 4.2 RESULTS AND DISCUSSION

### 4.2.1 Time Dependent Validation

Figure 4.2 shows the time-dependent temperature graph of the SWJ between the experiment and simulation. Due to the substantial temperature fluctuations in the experimental results, the collected data underwent a filtering process to achieve a smoother representation. In the results, the temperature curve can be divided into two phases: an unstable phase and a stable phase.

Figure 4.2 was explained by the law of conservation of energy. This graph is divided into Zone 1, Zone 2, and Zone 3, represented by the colors blue, green, and orange, respectively. During the initial phase, the chart was divided into Zone 1 and Zone 2. Zone 1 represents the heat absorption by the jacket material, aluminum. This heat absorption gradually decreases over time until it reaches a saturation state.

Consequently, the heat absorption taken by the water in Zone 2 increases to offset the diminishing impact of the aluminum. This means that during the unstable phase of Figure 4.2, the heat generation of the motor was absorbed simultaneously by the aluminum material and the flowing water inside. As the aluminum reaches its heat saturation state, the chart transitions into the stable phase. At this moment, the heat generation of the motor was solely removed by the water. This implies that the heat absorbed by the water corresponds to the heat generation of the motor, as demonstrated in Zone 3. According to the results, it can be observed that the temperature behavior of the simulation and experimental filter tends to be similar to each other in both stable and unstable phase.

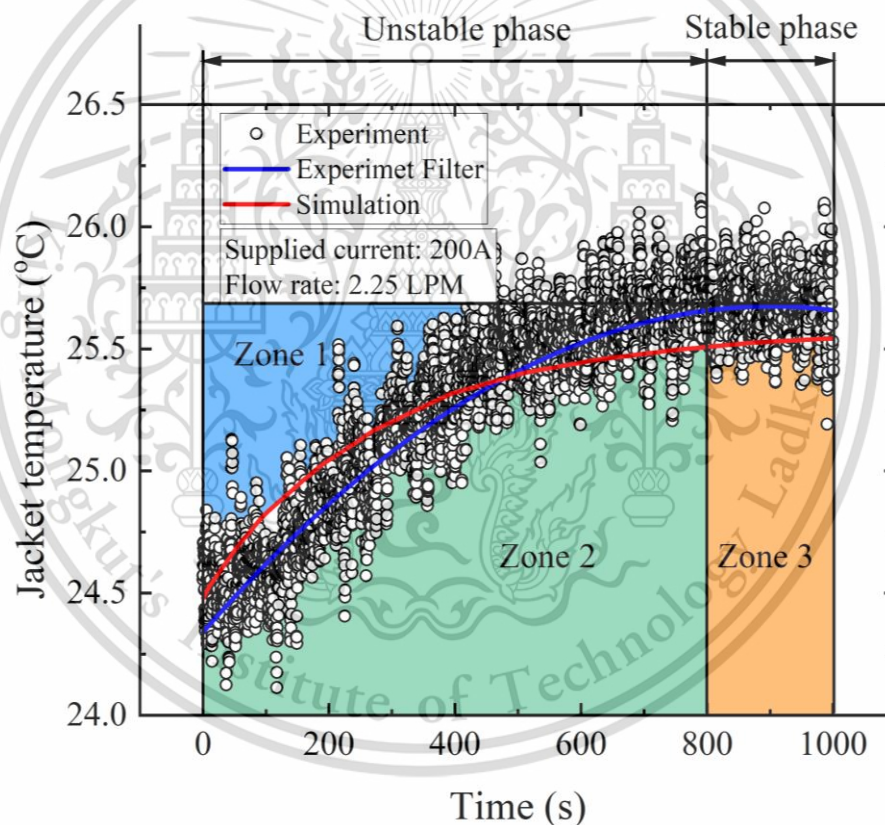


Figure 4.2 Jacket Temperature Comparison Between Simulation and Experiment.

#### 4.2.2 Stable State Validation of 3-key Parameters

This validation step has been conducted to simulate a stable state. The results were collected and compared with experiments conducted in Zone 3, as shown in Figure 4.2.

As detailed in Table 4.1, validation takes place with the main changes of three parameters that affect the cooling process: heat generation of the motor, inlet temperature, and flow rate.

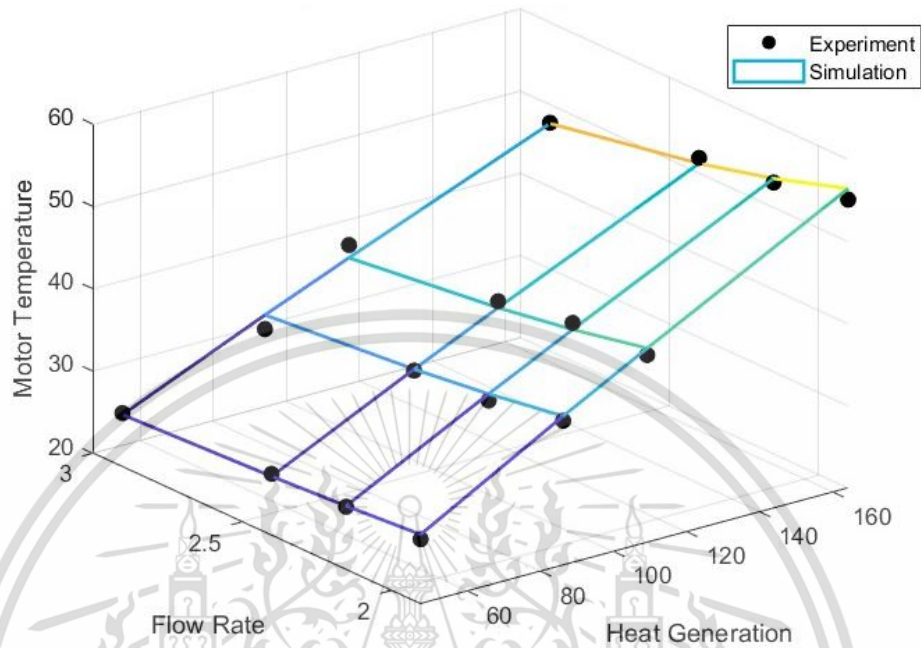


Figure 4.3 Validation of 3 Key parameters at Inlet Temperature of 19.65 °C.

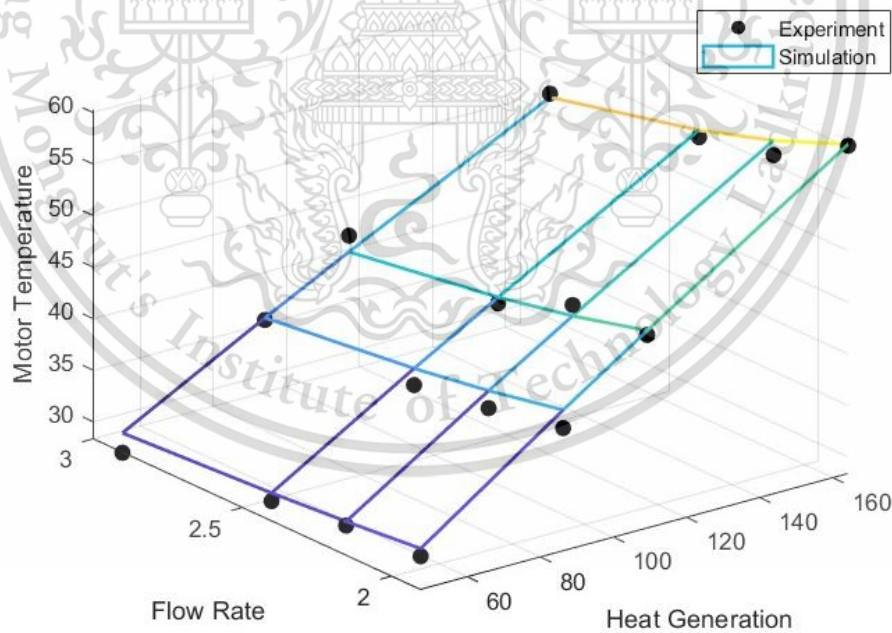


Figure 4.4 Validation of 3-key parameters at Inlet Temperature of 23.5 °C.

Figure 4.3 depicts the impact of heat generation and flow rate on maximum temperature of the motor at a certain inlet temperature of 19.65 °C. Absolute error (AE) is calculated based on Equation (2.10). The AE of motor heat generations of 47.01

W, 86.45 W, 109.32 W, and 164.27 W are 0.57 °C, 0.56 °C, 0.83 °C, and 1.35 °C, respectively. Similarly, at flow rates of 2.15 LPM, 2.4 LPM, and 2.9 LPM, the corresponding temperature errors for the same motor heat generations are 0.10 °C, 0.81 °C, 0.81 °C, and 0.49 °C; 0.30 °C, 0.17 °C, 0.79 °C, and 0.68 °C; and 0.20 °C, 1.71 °C, 1.55 °C, and 0.09 °C, respectively.

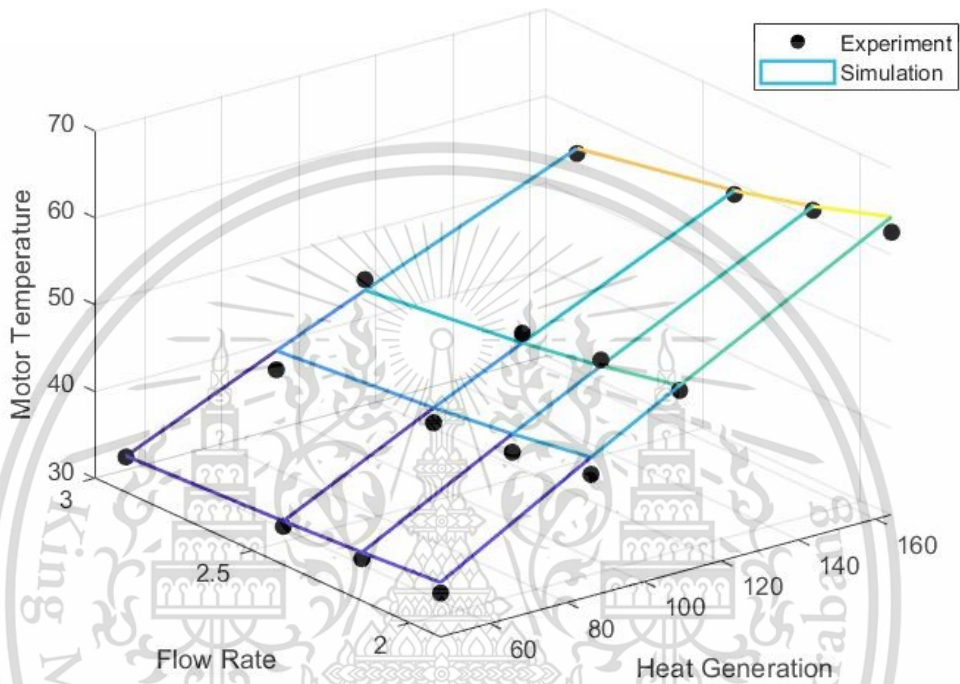


Figure 4.5 Validation of 3-key parameters at Inlet Temperature of 27.5 °C.

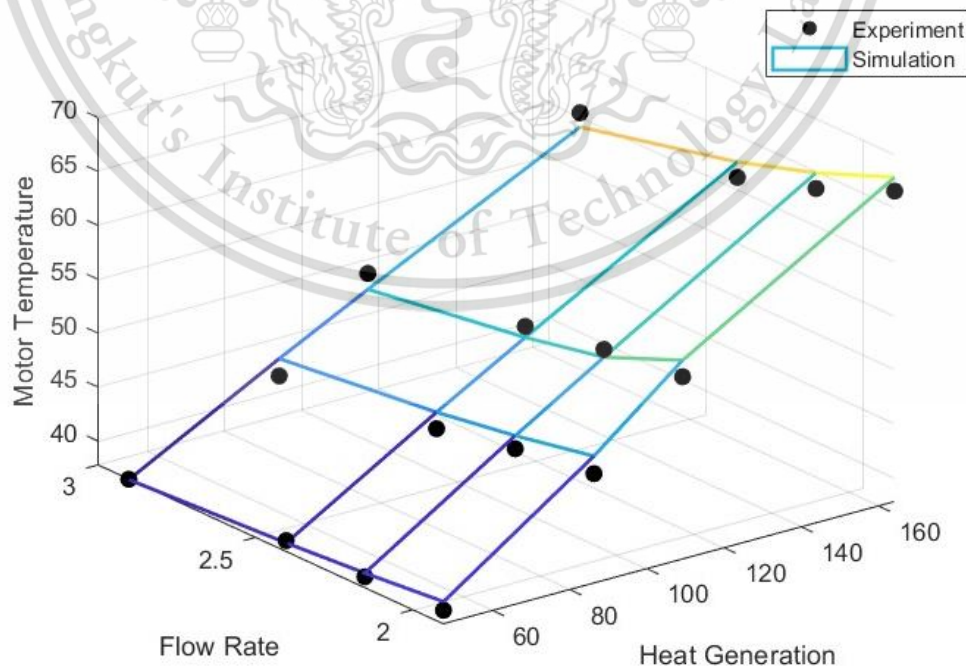


Figure 4.6 Validation of 3-key parameters at Inlet Temperature of 31 °C.

This material is reserved for educational use only, not allowed for commercial use.

Forbidden to modify the content, and cite the document when use.

In the inlet temperature condition of 19.65 °C, the maximum AE observed is 1.71 °C, and the minimum AE is 0.09 °C. Furthermore, the maximum relative error is 5.32 %, calculated based on the Equation (2.11).

Similarly, for inlet temperatures of 23.5 °C, 27.5 °C, and 31 °C, the maximum AE are 1.92 °C, 2.45 °C, and 1.63 °C, respectively. The minimum AE are 0.14 °C, 0.11 °C, and 0.04 °C, respectively. The RE are 6.77 %, 5.77 %, and 3.68 %, respectively.

The maximum RE of this model is observed to be 6.77% at an inlet temperature of 23.5°C, a flow rate of 2.9 LPM, and a motor heat generation of 47 W. This suggests that the highest error does not necessarily coincide with the highest heat dissipation level, indicating an independent relationship between the error and boundary conditions. This conclusion is supported by research conducted by Ryan Smith et al. [34]. In their study, the maximum error was reported as 9.94% at a winding dissipation of 862 W, while the maximum winding dissipation is 1070 W. Furthermore, this error is also 6.67% higher. However, the largest errors reported by Edison Gundabattini [10] and Chenglong Chu [35] were 5.4% and 4.6%, respectively, which are smaller than the 6.77% observed in this study. Nevertheless, it must be acknowledged that their validation process only extends to the time-dependent validation level, indicating lower comprehensiveness compared to this study.

#### 4.2.3 Temperature Distribution Validation

As Figure 3.1 described, the labels marked T1, T2, T3, and T4 as the circumference positions of motor winding from inlet to outlet. To make the validation process more comprehensive, simulation results were also collected at 4 similar locations to evaluate the accuracy of temperature distribution.

Figure 4.7 presents the comparison of the temperature between experimental and simulated results at 4-label positions. With a, b, c, and d representing the temperature distribution at peak currents of 100A, 135A, 170A, and 200A. All four cases are evaluated under an inlet temperature of 31°C and a flow rate of 1.9 LPM.

In Figure 4.7a, the experimental temperature is led by T4 at 40.48°C, followed by T3 and T2 at 38.6°C, and finally T1 at 38.53°C. Additionally, the simulated temperature of T4 and T3 both stand at the top with 40.06°C, followed by T2 at 39.81°C, and T1 at the bottom with 39.46°C. Based on Equations (2.10) and (2.11), both

absolute error (AE) and relative error (RE) were also calculated in this instance. The maximum AE and RE were observed for T3 at 1.46°C and 3.78%, respectively, while the minimum AE and RE were recorded for T4 at 0.42°C and 1.03%, respectively.

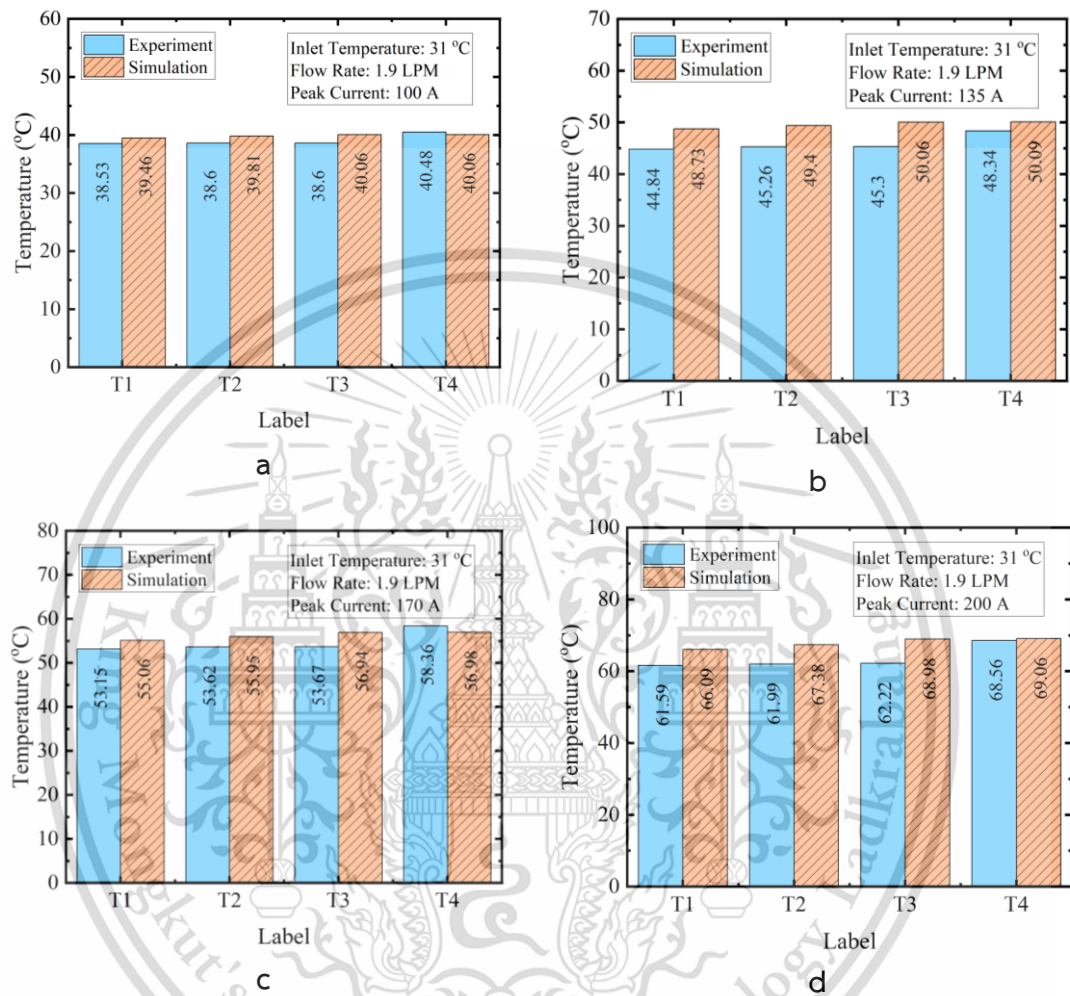


Figure 4.7 Validation of Four Positions Along Circumference from Inlet to Outlet

In Figure 4.7b, the maximum and minimum values of AE and RE persisted steadily at labels 3 and 4. Specifically, T3 exhibited an AE of 4.8°C and an RE of 10.6%, while T4 showed an AE of 1.74°C and an RE of 3.6%.

In Figure 4.7c, T3 maintained its position with the highest AE and RE values at 3.32°C and 6.16%, respectively. Similarly, T4 remained consistent as it attained the lowest AE and RE values at 1.38°C and 2.36%, respectively.

As predicted, in Figure 4.7d, T3 had the highest AE and RE values with 6.99°C and 11.28%, respectively, while T4 had the lowest AE and RE values with 0.5°C and 0.73%.

The maximum relative error is quite high, 11.28%. Because the fact that the initial temperature of the motor without cooling was not uniform across different points in the winding, shown in Figure 4.8. This is due to the motor operating for an extended period, causing the quality of the insulation layer to deteriorate.

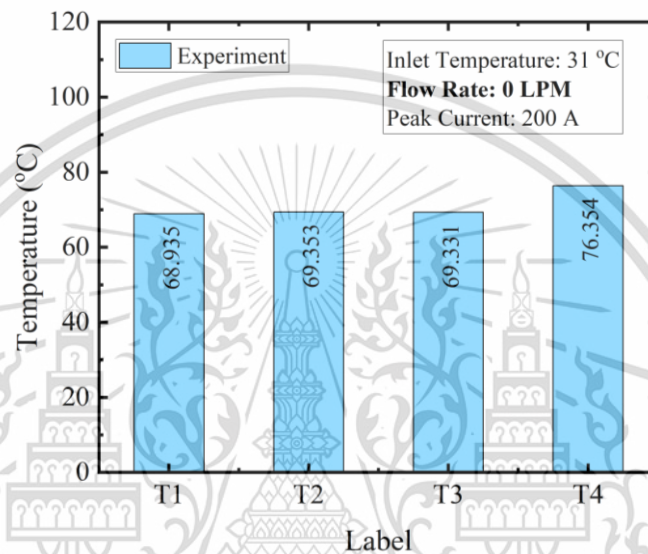


**Figure 4.8 Winding Temperature without Cooling**

Overall, the cases described in Figure 4.7 exhibit similarities in temperature distribution. Specifically, the temperature gradually increases from T1 to T4, indicating a gradual rise from the inlet to the outlet, as initially predicted. These results also align with the findings of Hendrik Vansompel and Peter Sergeant's study [36].

## CHAPTER 5

## PART III: COMPARISON OF WATER-COOLING JACKETS

## 5.1 RESEARCH METHODOLOGY

## 5.1.1 Designs for Water-cooling Jackets

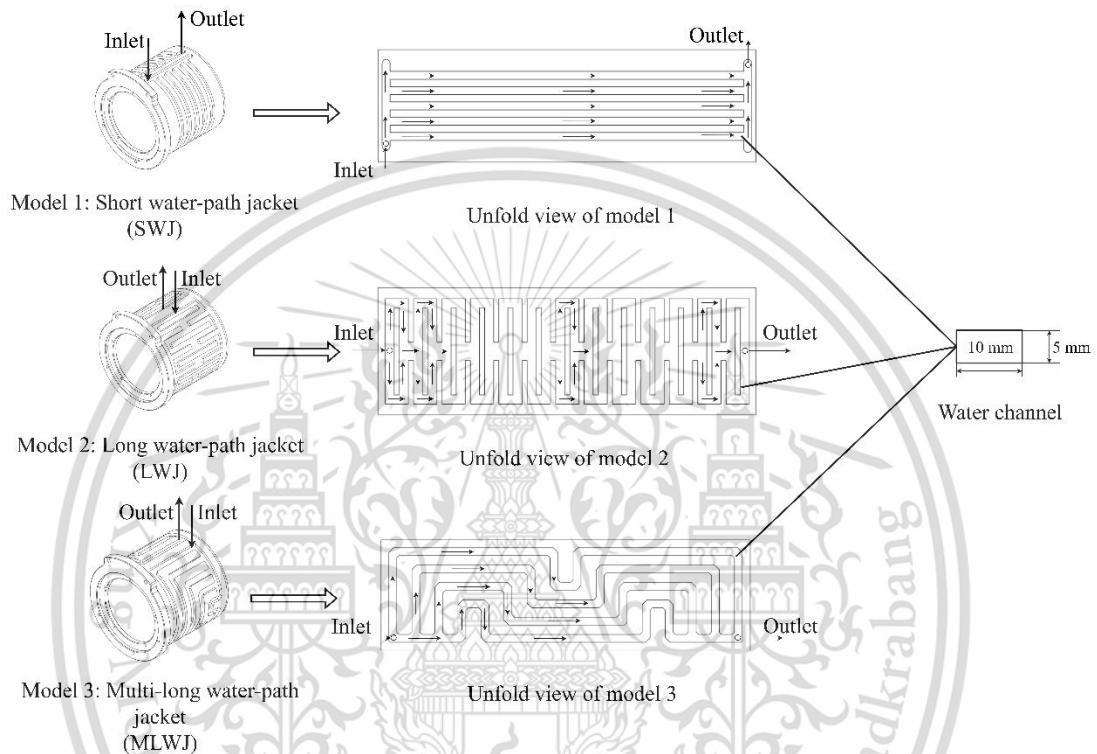


Figure 5.1 Detailed Topology Comparison of Three Designs

If Figure 5.4 illustrated the structure of the water-cooling jacket (WJ) cooling system, consisting of the jacket cover and the topology of the water-cooling jacket, in this chapter, the topology of the water-cooling jacket will be explored, analyzed, and compared. The detailed design of the three topology models presented in Figure 5.1.

In addition to laminar flow rate, topology also significantly impacts the cooling performance of a system. In this chapter, Model 1, Model 2, and Model 3, named short water-path jacket (SWJ), long water-path jacket (MLWJ), and multi-long water path jacket (MLWJ), respectively, are evaluated and compared.

- Model 1: This structure is the simplest among the 3 models. The inlet is designed longitudinally to distribute water to each channel, with 5 circumferential branches flowing from the inlet to the outlet. Subsequently, water from the channels converges at the outlet and

This material is reserved for educational use only, not allowed for commercial use.

Forbidden to modify the content, and cite the document when use.

flows longitudinally. This design features 5 short branches, flowing directly from the inlet to the outlet without any serpentine. The position of the inlet and outlet ports located at 2 corners may lead to uneven distribution of water content among the channels.

- Model 2: Unlike the other 2 models, this design stands out with interconnections between channels allowing for heat exchange among the water channels. Due to the inlet and outlet ports positioned at the center, the distribution of water content among the channels is more even. The hottest spot of a motor is typically at the center due to low contact with the external environment, and the junctions between the 2 outer channels create a third water channel, main channel, shortcutting directly from the inlet to the outlet, aiding in optimal cooling at the center of the motor. The two outer channels winding in serpentine patterns increase the heat exchange time of the water content with the motor.
- Model 3: This design shares many similarities with Model 1, with 5 independent channels connecting from the inlet to the outlet, and the inlet and outlet ports located at the corners of the water channels. Additionally, this model resembles Model 2 in its serpentine pattern, but lacks heat exchange between channels. Model 3 is a compromise between the distinctive features of the other two models.

### 5.1.2 Simulation Setup

A 3D model has been created based on the actual motor as depicted in Figure 5.2 and Figure 5.3. The purpose of this 3D model is to enable comparative evaluation without the need for physical fabrication, thereby reducing costs and optimizing the process.

The WJ comprises two primary components: a water-cooling jacket topology and a jacket cover. It is designed as an external enclosure surrounding the motor, as depicted in Figure 5.4. As mentioned earlier, this cooling system is of a type that does not involve any intervention or modification of the original design of the motor.

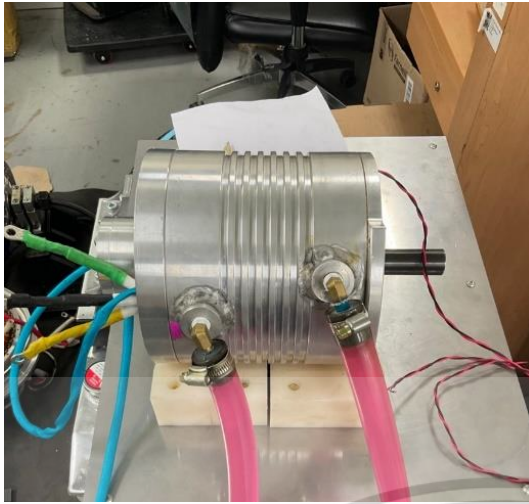


Figure 5.2 Installation of Water-Cooling Jacket and Motor.

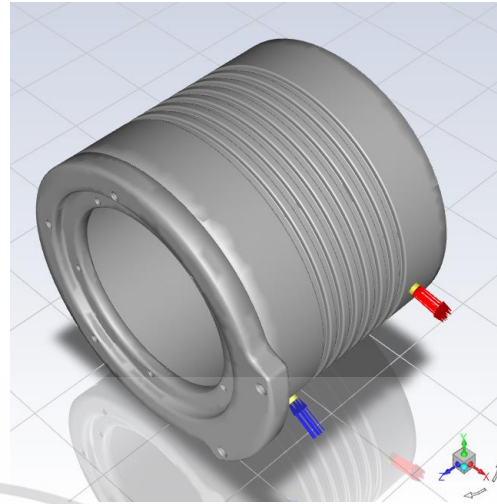


Figure 5.3 3D-modeling of motor.

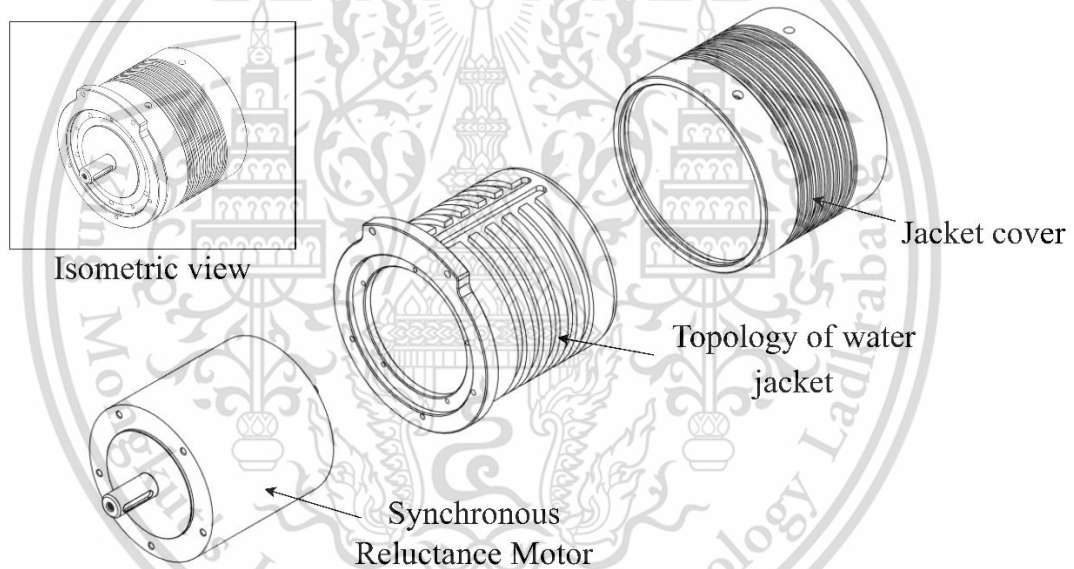


Figure 5.4 Exploded View of Motor-water-cooling jacket Combination.

The input parameters used for the simulation include the heat generation of the motor, the flow rate of the coolant, and the inlet temperature of the radiator. These parameters were collected through experiments. However, the heat transfer coefficient was obtained from the material library, calculated as Equation (5.1). The apparent heat transfer coefficient from the experiment will be used to evaluate the model after simulation.

$$HTC = \frac{N_u \cdot k}{L_d} \quad (5.1)$$

where  $N_u$  is the Nusselt number, which depends on the flow conditions and geometry,  $k$  is the thermal conductivity,  $L_d$  is the characteristic length.

Because the cooling channel in this design is rectangular, the Nusselt number is calculated as Equation (5.2) with Reynolds number ( $R_e$ ) and Prandtl number ( $P_r$ ).

$$N_u = 0.664 \cdot R_e^{0.5} \cdot P_r^{1/3} \quad (5.2)$$

The Reynolds number and Prandtl Number are calculated based on water properties such as the density of the fluid ( $\rho$ ), velocity ( $v$ ), dynamic viscosity of the fluid ( $\mu$ ), and the specific heat capacity ( $C_p$ )

$$R_e = \frac{\rho \cdot v \cdot L_d}{\mu} \quad (5.3)$$

$$P_r = \frac{\mu \cdot C_p}{k} \quad (5.4)$$

### 5.1.3 Grid independent technique.

Mesh specification is considered one of the crucial factors influencing the computational results of the finite element method [37]. To ensure the reliability of the simulation, The grid independence method is used to verify the independence of the mesh with respect to simulation results [38]. The SWJ was chosen as the reference model to assess mesh quality. Figure 5.5 depicts the input parameters and boundary conditions, which include the maximum motor heat generation of 119.63 W, a flow rate of 2.25 LPM, and a maximum inlet temperature of 24.45°C. The impact of mesh on the maximum temperature of the WJ, as depicted in Figure 5.6, was assessed by dividing it into three different element counts to facilitate comparative simulations. The maximum jacket temperatures recorded with 28486 elements, 48936 elements, and 95244 elements were 25.7 °C, 25.53 °C, and 25.54 °C, respectively. The temperature difference between the latter two element counts was relatively minor, just 0.01 °C. Consequently, it is evident that the simulation results became independent of the element count when exceeding 48936 elements. Therefore, the model with a mesh quality of 95244 elements was chosen for further calculations.

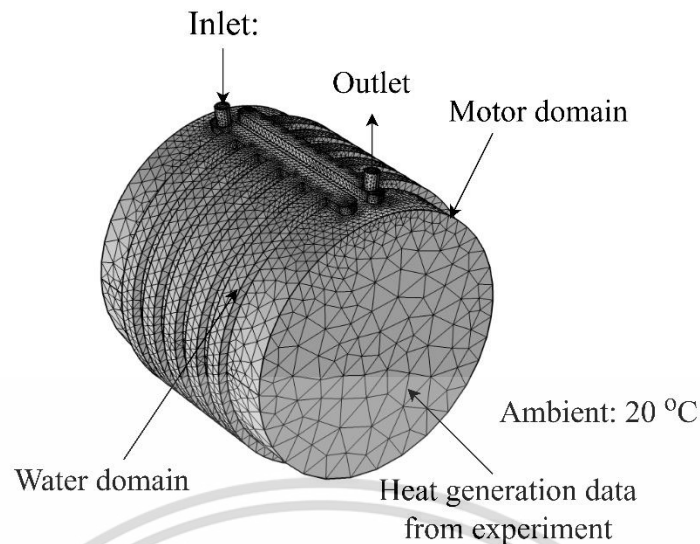


Figure 5.5 Meshing Setup of 3D-modeling.

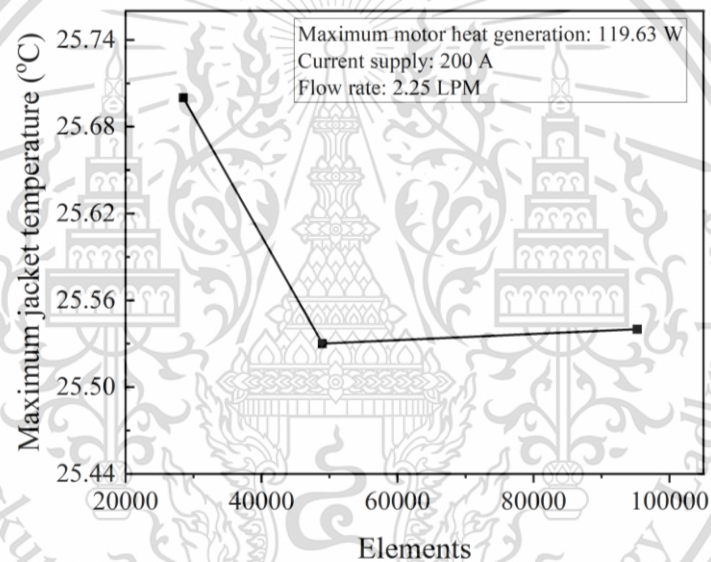


Figure 5.6 Relationship Between Temperature and Element Numbers

#### 5.1.4 Step-running Technique.

To optimize computational resources and increase processing speed, a step running approach, as described in Figure 5.7, is employed. This technique involves computing separate models into two domains: the water domain and the solid domain. Water domain and solid domain were inserted input parameters for fluid and solid, modeled as laminar flow components and heat transfer components, and computed using stationary and time-dependent studies, respectively. In this approach, the results of the stationary study serve as the initial condition for the time-dependent study. The results of the time-dependent study

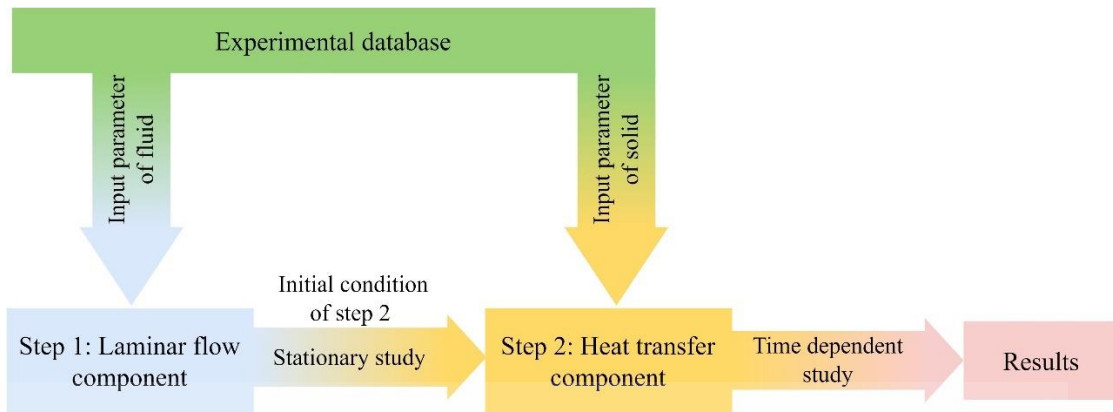


Figure 5.7 Step-running of Simulation Process.

### 5.1.5 Boundary Condition

These 3 models are evaluated under the same boundary conditions, selected as a current supply of 200A and an inlet temperature of 19.65°C. This boundary condition is chosen because it falls under one of the validation conditions presented in Table 4.1, ensuring high reliability, and it represents one of the most extreme operating conditions for the motor. The more severe the conditions, the clearer the differences between the models become. As for the flow rate, in the next chapter, the pump control strategy will be evaluated and researched. Since the flow rate will vary during the cooling process, in the evaluation of different topologies, flow rates will be used as a variable.

## 5.2 RESULTS AND DISCUSSIONS

### 5.2.1 Effect of Flow Rate on Cooling Jacket Model

In Figure 3.11 and Figure 3.12, we also observe that, although the temperature decreases significantly with increasing flow rate, the decrease in temperature is not as pronounced between low and high flow rates. In this results section, we will analyze the effect of flow rate on the average temperature of the motor more clearly. Figure 5.8 illustrated the effect of flow rate on the average temperature of all three motor models, with an increase step of 1 LPM.

This result was evaluated under the condition that the motor was supplied with a current of 200 A, the inlet temperature was fixed at 19.65 °C, and the collected temperature represents the average temperature of the motor.

At a flow rate of 1 LPM, the average temperature of Model 1 ranked first at 78.85 °C, followed by Model 3 with 79.72 °C, and finally Model 2 with 74.17 °C. With a subsequent increase in flow rate of 1 LPM, the average temperature of motor models 1, 2, and 3 decreased by 24.09 °C, 23.39 °C, and 25.04 °C, respectively.

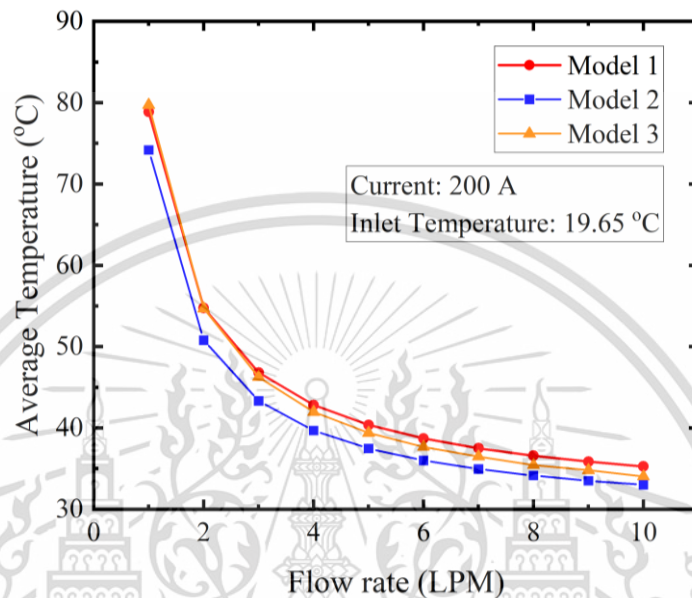


**Figure 5.8 Effect of Flow Rate on Average Temperature of Motor.**

At 2 LPM, Model 1 remains the highest with a temperature of 54.68 °C, followed closely by Model 3 at 54.67 °C, and Model 2 at the lowest with 50.78 °C. However, upon further increasing the flow rate, the temperature decrease is marginal, with Model 1, Model 2, and Model 3 decreasing by 7.95 °C, 7.47 °C, and 8.43 °C, respectively. This indicates that further increasing the flow rate does not significantly reduce the temperature anymore. To balance water pumping effort and cooling efficiency, 3 LPM was chosen as the optimal flow rate.

### 5.2.2 Temperature Difference

In Figure 5.9, the relationship between the flow rate of coolant and temperature difference in the same model is presented. At 1 LPM, the temperature difference of Model 2 leads with 7.2 °C, followed by Model 1 with 4.61 °C, and finally Model 3 with 4.52 °C.

With a 1 LPM increase in the flow rate, the temperature difference of Model 2 dropped by 3.02 °C while still maintaining the leading position with 4.18 °C. Model 3

decreased by 1.4 °C, rising to second place with 3.11 °C, and Model 1 decreased by 1.78 °C, falling to the last position with 2.83 °C.

With another 1 LPM increase, the positions of the models remain unchanged. Model 2 maintains the lead, decreasing by 1.19°C to 4.18°C. Model 3 stays in second place, decreasing by 0.8°C to 3.11°C, while Model 1 remains at the bottom, decreasing by 0.74°C to 2.83°C.

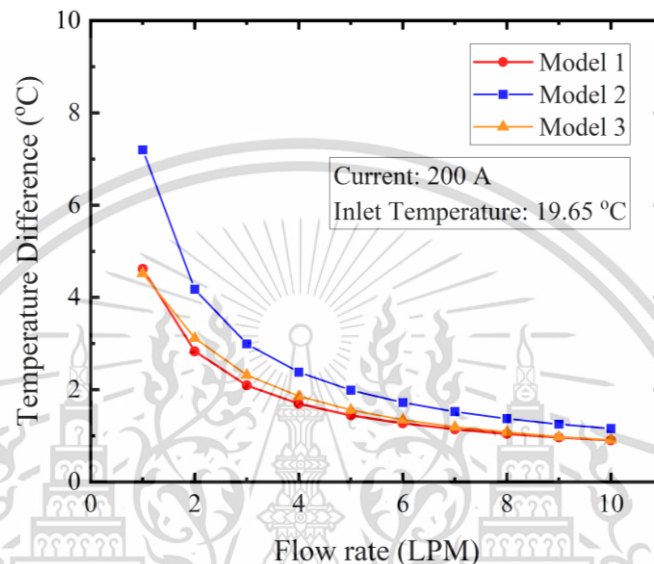


**Figure 5.9 Effect of Flow Rate on Temperature Difference in 3 Models**

In general, the positions of the models in terms of temperature difference remain unchanged until the final simulation condition of 10 LPM. The temperature difference curves of Model 1 and Model 3 are low and relatively similar. This may be due to the common characteristic of many water paths and the channels being independent of each other, which allows for propagation across the wide area of the water channels, thereby reducing the temperature difference. This explanation is supported by the research of Bin Zhang et al. [39], whose study demonstrated that increasing the number of water channels results in a rapid increase in the convection heat transfer coefficient, thereby enhancing widespread temperature diffusion.

In addition, as the flow rate increases, the temperature difference tends to decrease, similar to the results shown in Figure 5.8. At 3 LPM, which is also a threshold flow rate, if surpassed, the temperature decrease is slight rather than significant.

However, it is worth noting when comparing the results in Figure 5.9 and the results in Figure 5.8, Model 1 has the highest average temperature but the lowest

temperature difference, while Model 2, with the lowest average temperature, has the highest temperature difference.

Unlike other studies that focus on the average or maximum temperature of the motor [40, 41], this study emphasizes the analysis of temperature variance. This is because a design with a low average temperature, but a large temperature variance can lead heat to concentrate in a specific area of the motor, leading to localized damage.

### 5.2.3 Pressure Drop

Apart from temperature, increasing the flow rate also affects the pressure drop, as depicted in Figure 5.10.

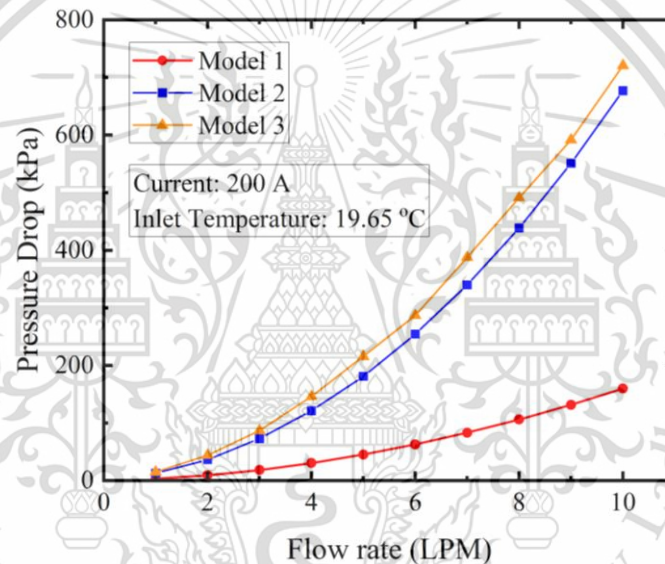


Figure 5.10 Effect of Flow Rate on Pressure Drop with Differential Models

At 1 LPM, Model 3 leads with a pressure drop of 14.75 kPa, followed by Model 2 with 12.5 kPa, and finally Model 1 with 3.03 kPa. When increasing by another 1 LPM, Model 1 continues to be the highest, significantly increasing by an additional 29.19 kPa to 43.94 kPa, followed by Model 2 increasing by an additional 23.75 kPa to 36.27 kPa, and finally Model 3 increasing by an additional 6.05 kPa to 9.07 kPa.

At 3 LPM, Model 3 continues to lead, increasing to 86.62 kPa, followed by Model 2 increasing to 72.61 kPa, and finally Model 1 increasing to 18.2 kPa. Then, the flow rate continues to increase, leading to a significant increase in the pressure drop of all three models. The relationship between increasing flow rate and the corresponding increase in pressure drop is consistent with the findings in the study by E. Fantin Irudaya Raj et al. [1].

This material is reserved for educational use only, not allowed for commercial use.

Forbidden to modify the content, and cite the document when use.

As analyzed in Figure 5.8, beyond 3 LPM, the increase in flow rate does not result in a significant temperature reduction. Instead, it leads to considerable power consumption by the water pump. To be clearer, Figure 5.11 shows that pump work increases in proportion to the pressure drop because it is calculated based on the pressure drop and the constant volume of the water jacket. When multiplied by the time unit, it represents power consumption. At this stage, the ranking of the three models has changed concerning pump work. Model 1 remains in the lead, followed by Model 3, with Model 2 ranking last.

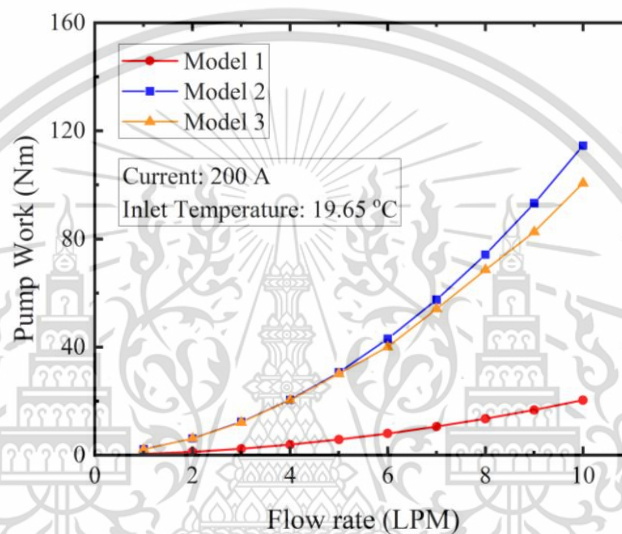


**Figure 5.11 Pump Work of Three Different Models as Flow Rate Increases**

Additionally, jacket topology also significantly influences the pressure drop. Specifically, the topologies of LWJ (Model 2) and MLWJ (Model 3) exhibit much higher-pressure drops compared to SWJ (Model 1). This is explained by the serpentine pattern of LWJ and MLWJ, which includes multiple bends that increase the pressure on the pump.

#### 5.2.4 Effect of Water Path on Temperature Distribution

Temperature distribution of SWJ, LWJ, and MLWJ is illustrated in Figure 5.12, Figure 5.13, and Figure 5.14, respectively. Overall, all three water-cooling jackets (WJs) exhibit a gradual increase in temperature from the inlet to the outlet. However, in the SWJ, there is a difference in temperature along the vertical direction of motor between areas in contact with the cooling channel and those that are not. MLWJ also shows a similar temperature distribution. In contrast, LWJ has a more uniform temperature

distribution. This can be explained by the water content exchange between channels of LWJ, leading to better diffusion and heat exchange.

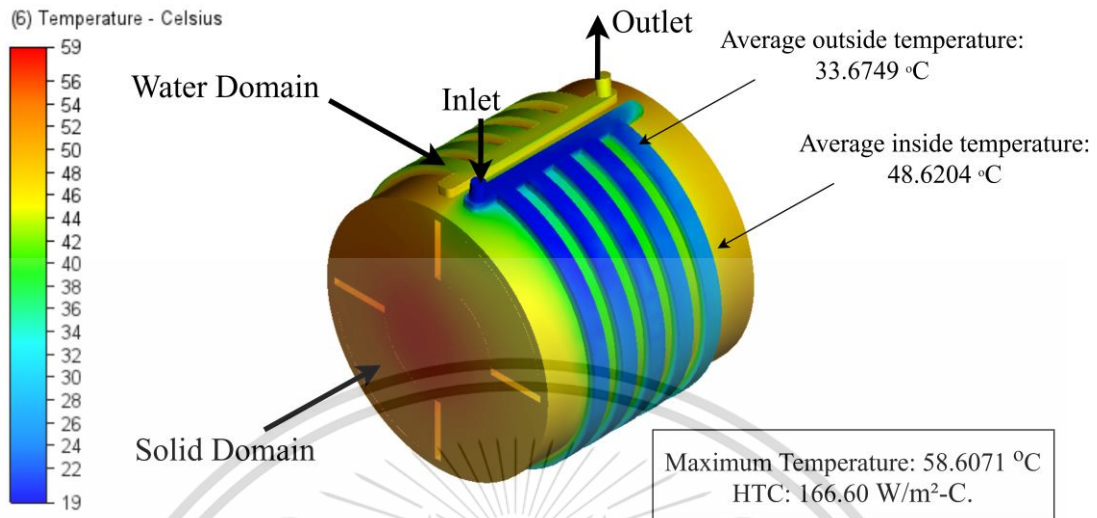


Figure 5.12 Temperature Distribution of SWJ

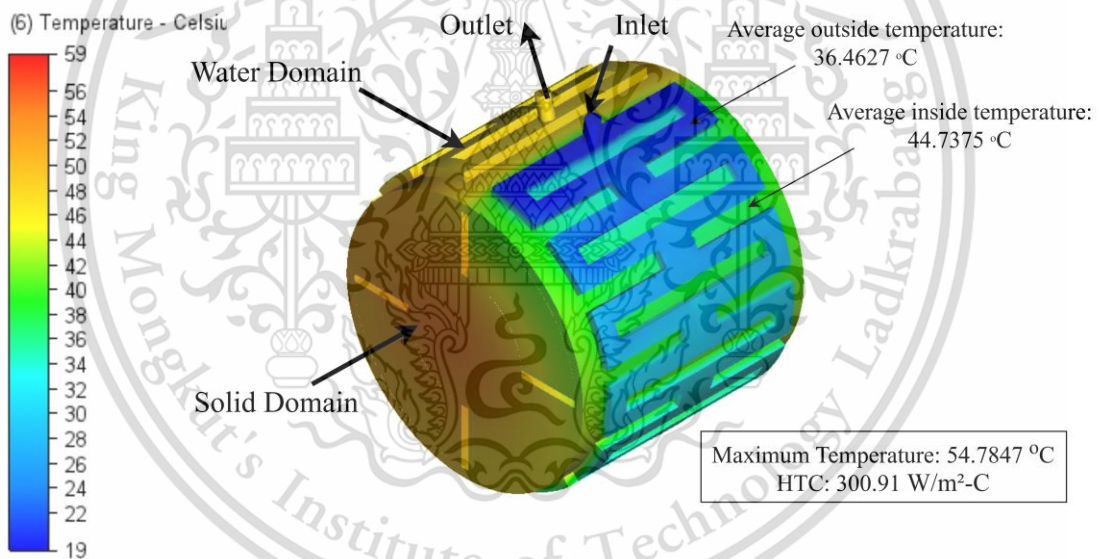


Figure 5.13 Temperature Distribution of LWJ

Observing all three models, it can be seen that LWJ exhibits a smaller difference in color representing the temperature of the solid domain and water domain compared to the other two models. According to Equation (3.2), the HTC of LWJ is higher than that of SWJ and MLWJ. This explains why the maximum temperature of LWJ is the lowest among the three models. Additionally, the HTC in this result differs from the convection heat transfer coefficient explained in the temperature difference section. The HTC in this result represents the heat transfer from the motor to the WJ rather than between the water channels themselves.

This material is reserved for educational use only, not allowed for commercial use.

Forbidden to modify the content, and cite the document when use.

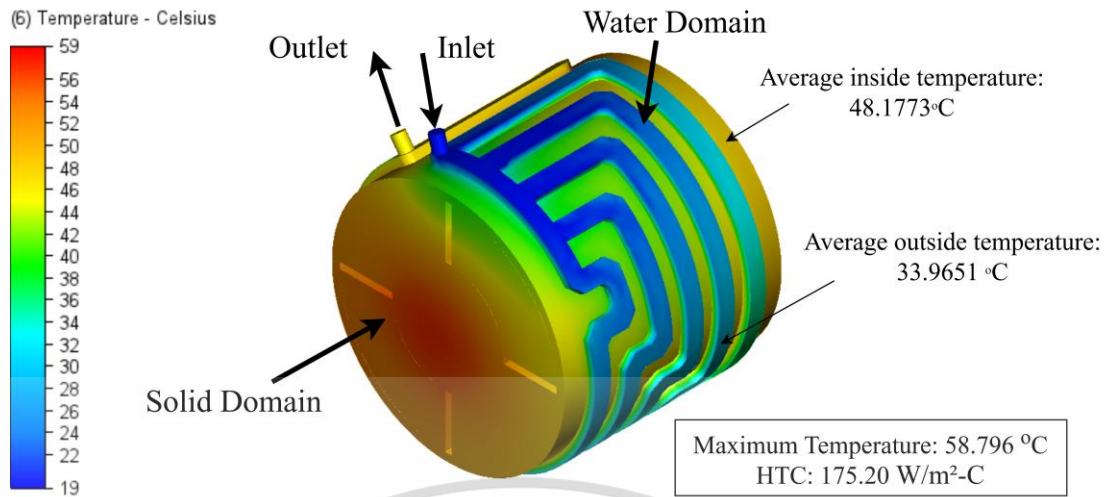


Figure 5.14 Temperature Distribution of MLWJ

In addition, it can be observed that MLWJ stands out compared to the other two models with a more uniform temperature distribution of the motor along the circumferential direction from inlet to outlet.

### 5.2.5 Ranking of Water-cooling Jacket

Table 5.1 Ranking of Water-cooling Jackets

	Average Temperature	$\Delta T$	Maximum Temperature	Pump work	Conclusion
Model 1: SWJ	3rd	1st	2nd	1st	Good economic and technique
Model 2: LWJ	1st	3rd	1st	3rd	Good performance
Model 3: MLWJ	2nd	2nd	3rd	2nd	Not passed

Figure 5.8 shows that the gap between Model 2 and the other models remains constant over the flow rate. This means that no matter how much the flow rate increases, Model 2 still stands out in cooling performance. However, when observing Figure 5.9 and Figure 5.10, the gap between Model 2 and the other models decreases and increases with increasing flow rate, respectively. This means that the temperature difference and pressure drop can be adjusted based on the optimal flow rate. This chapter focuses on effective design, so Model 2 is the most optimal model in this aspect.

## CHAPTER 6

### PART IV: COOLING STRATEGY

#### 6.1 RESEARCH METHODOLOGY

##### 6.1.1 Training Data Collection

After comprehensive validation, the accuracy of the 3D model has been confirmed. Now, the 3D model is utilized for simulating 1000 cases, covering three key parameters: heat generation of the motor, inlet temperature, and flow rate, as outlined in Table 6.1.

**Table 6.1 Training Cases**

No	Torque (Nm)	Inlet Temperature (°C)	Flow Rate (LPM)
1	1	19.5	1
2	2	21	2
3	3	22.5	3
4	4	24	4
5	5	25.5	5
6	6	27	6
7	7	28.5	7
8	8	30	8
9	9	31.5	9
10	10	33	10

In training cases, the motor torque oscillates within the range of 1 to 10, based on the motor characteristics referenced in Table 2.1. As outlined in the validation chapter, the inlet temperature is chosen based on the actual temperature conditions of Southeast Asia. However, in the training case, the inlet temperature is restricted to a broader range, from 19.5°C to 33°C. The results from Figure 5.8 and Figure 5.10 indicated that increasing to high flow rates does not significantly reduce temperature. This material is reserved for educational use only, not allowed for commercial use.

Forbidden to modify the content, and cite the document when use.

but notably increases pump power, as evidenced by the pressure drop. Therefore, during training, flow rates are only collected within the range of 1 to 10 LPM.

The simulation results collected are the average temperature of the motor. These results serve as the supervisor answer for the training steps of the subsequent neural network.

### 6.1.2 Training Setup

Training processes were conducted on a laptop computer with the following hardware specifications.

- Processor: AMD Ryzen 7 6800H
- Memory: 16 GB DDR5
- Display 1: AMD Radeon™ Graphics
- Display 2: NVIDIA GeForce RTX 3050Ti
- Storage: 512 GB SSD M.2 NVMe PCIe Gen4

Training and simulation were performed using the following software and tools:

- Operating System: Windows 11 Education
- Programming Languages: Matlab
- Simulation Environment: Matlab/Simulink
- Framework: Neural net fitting

Figure 6.1 provided an overview of the training process involving two models. One model predicts the average temperature of the motor based on parameters such as motor torque, inlet temperature, coolant flow rate, and ambient temperature. Among these, the ambient temperature remains constant, while the other parameters serve as inputs for training ML model 1, with temperature serving as the supervisor answer.

ML model 2 also employs the supervisor answer method for training, functioning as a decision model. Its input parameters shift from flow rate to the average temperature of the motor, which is the output of ML model 1. Consequently, the output of ML model 2 becomes the flow rate used to control the pump, while also serving as feedback data for ML model 1.

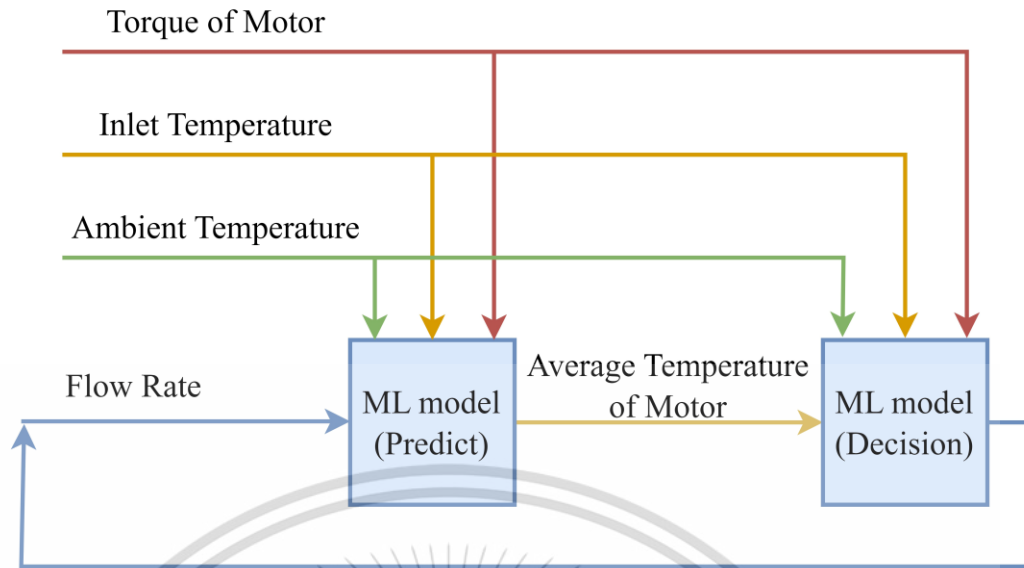


Figure 6.1 Schematic Diagram of Training Process

The decision tree is used to learn from historical data and make decisions in the future. This prediction involves establishing rules based on historical data and applying them to new data. These rules are typically represented hierarchically [42]. The training process described in the decision tree, as shown in Figure 6.2, involves to training for ML model 1, aimed at predicting the average temperature of the motor.

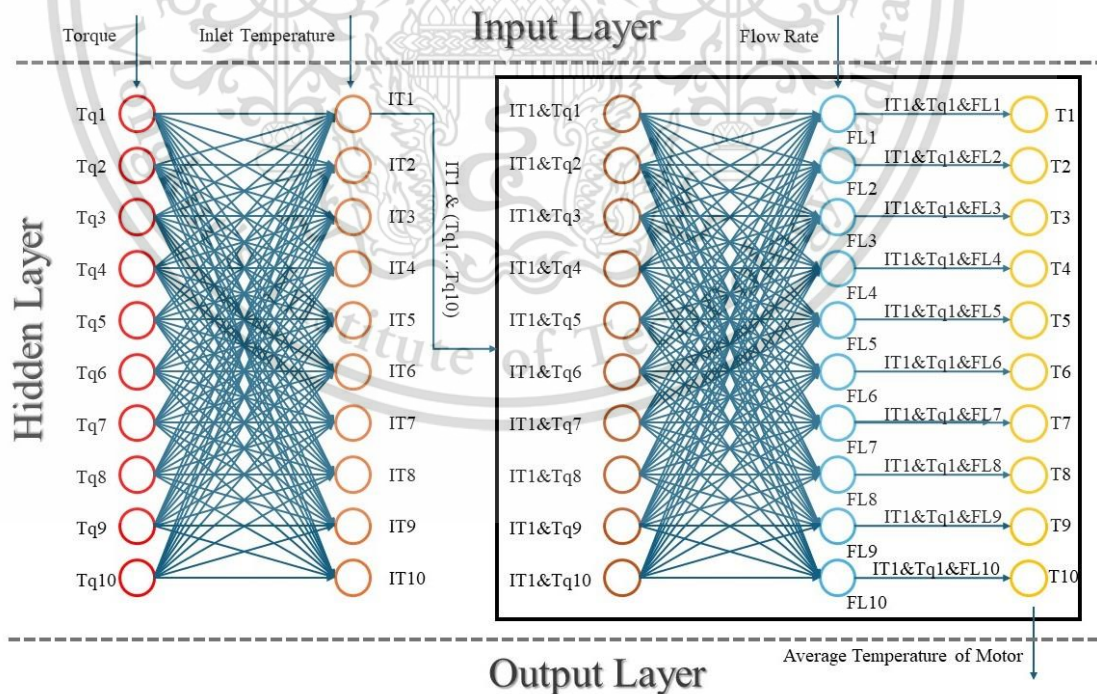


Figure 6.2 Decision Tree of Neural Network for Stable State Heat Equation

Each artificial neural network is a multilayer perceptron, a neural network consisting of an input layer, an output layer, and hidden layers. The input layer comprises three parameters: motor torque, inlet temperature, and water flow rate. The motor torque has 10 values labeled Tq1 to Tq10, the inlet temperature is labeled IT1 to IT10, and the water flow rate is labeled FL1 to FL10. All of these values are considered network nodes and act as sigmoid neurons.

From left to right, each sigmoid neuron Tq1 to Tq10 is connected to 10 sigmoid neurons from IT1 to IT10. As a result, each sigmoid neuron from IT1 to IT10 has established 10 connections called IT1&Tq1 to IT1&Tq10, IT2&Tq1 to IT2&Tq10, ..., IT10&Tq1 to IT10&Tq10. To simplify understanding, Figure 6.2 only illustrates the neural network at the sigmoid neuron IT1. At this point, the number of neural connections has increased to 100. Afterward, they further connect to sigmoid neurons from FL1 to FL2, increasing multiplicatively from 100 to 1000. One of the outcomes of predicting the average temperature of the motor will emerge from these 1000 connections.

The neural network of ML model 2 is similar to model 1, differing only in the input parameter, where the flow rate value is replaced with the average temperature of the motor. The output of ML model 2 is the flow rate of water.

### 6.1.3 Vehicle Dynamics in MATLAB/Simulink

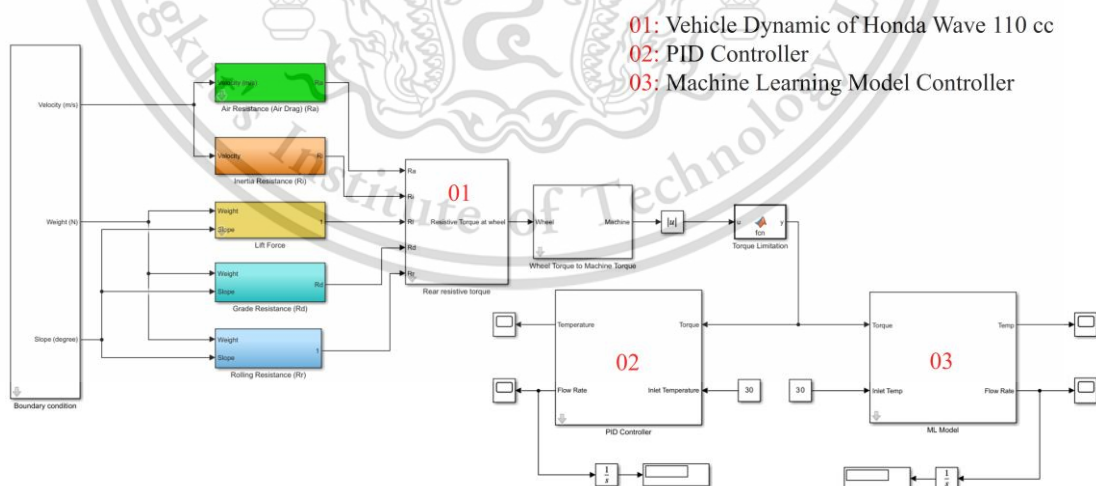


Figure 6.3 Block Diagram of Simulink Environment

- Schematic of power train system

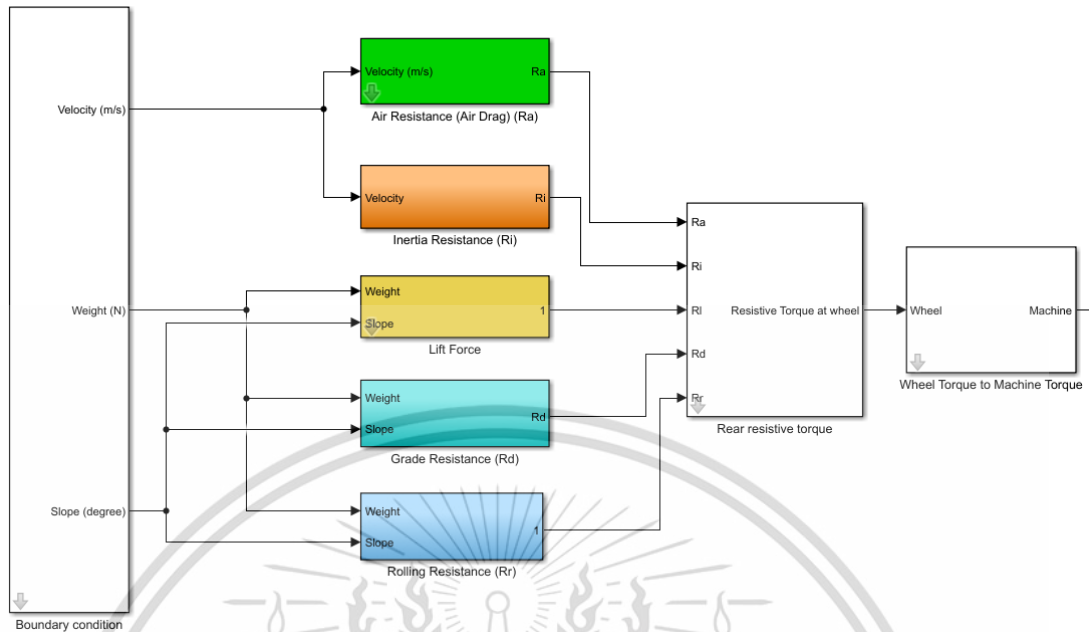


Figure 6.4 Power Train System

Figure 6.5 presents the powertrain system with the vehicle's resistance forces mathematically modeled. These resistance forces include aerodynamic resistance, grade resistance, rolling resistance, inertial resistance, and lift force, based on Equation (2.4), Equation (2.6), Equation (2.7), Equation (2.8), and Equation (2.9), respectively.

- Logical PID

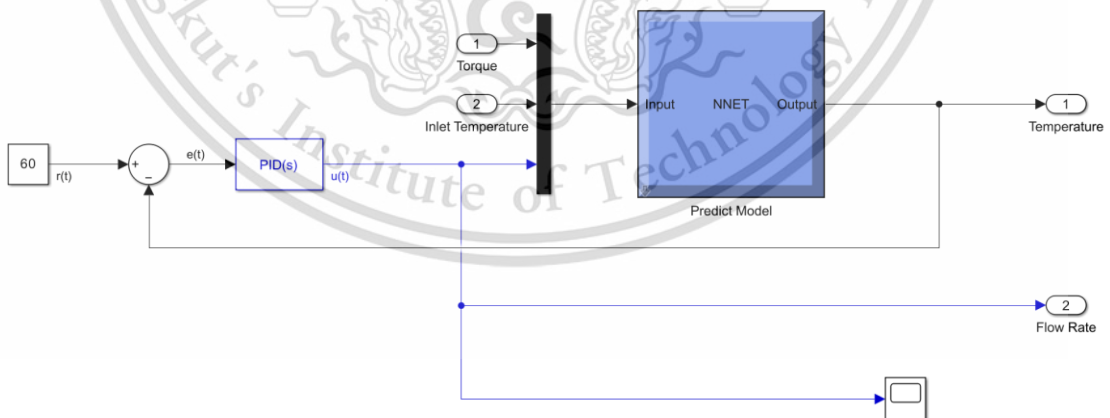


Figure 6.5 Applying PID in Controller

The Logical PID is used to compare ML models in the control strategy. The ML model predicting temperature serves as the position of the transfer function in the conventional PID diagram. ML model 1 was selected because

it is constructed based on real-world test conditions, providing an objective evaluation, as depicted in Figure 6.5.

- Cluster of ML models.

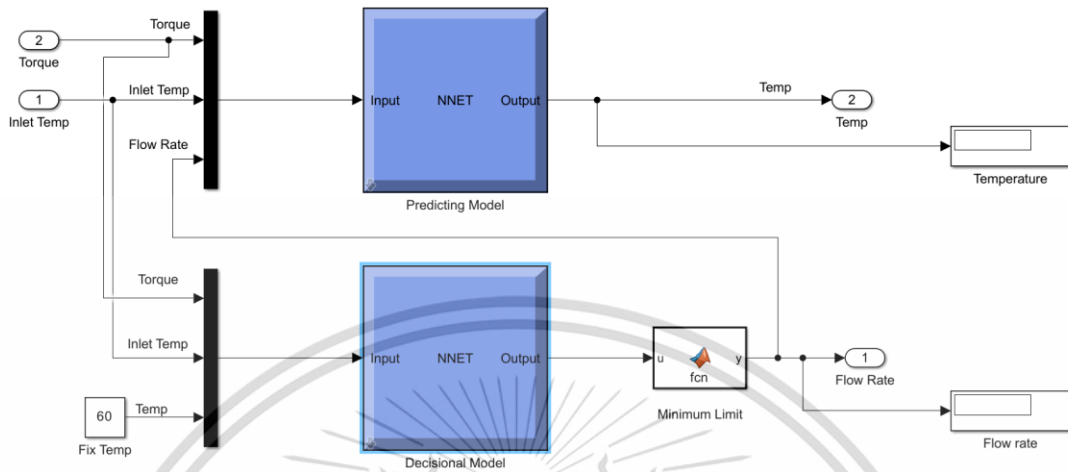


Figure 6.6 Applying ML Model in Controller

The prediction model remains in use for motor temperature prediction. However, this time, it involves a combination of the results from two ML models, where the prediction outcome serves as input parameters for the control model. Subsequently, the control result becomes feedback for the prediction model. The two models complement each other in their operation. Diagram of 2 ML model connection is expressed in Figure 6.6.

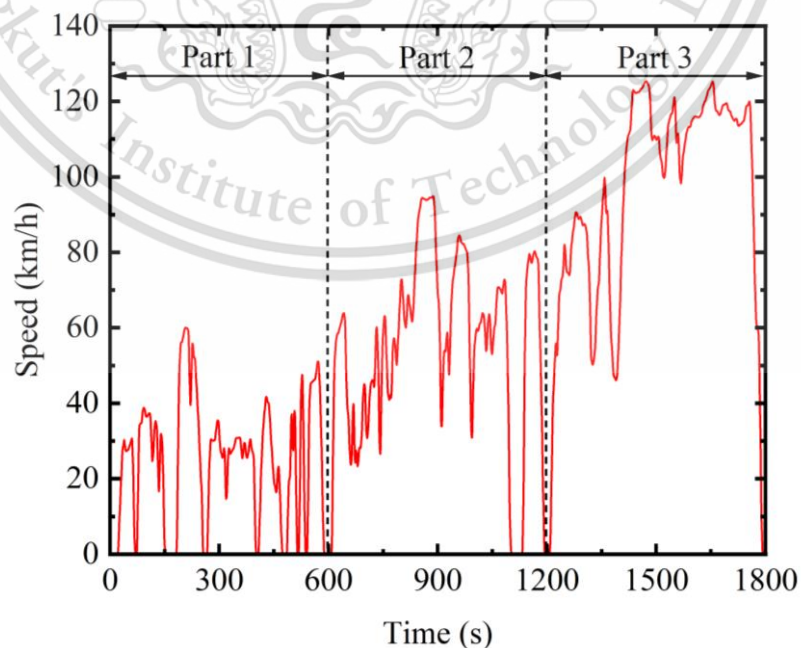


Figure 6.7 World Motorcycle Test Cycle Singal

This material is reserved for educational use only, not allowed for commercial use.

Forbidden to modify the content, and cite the document when use.

- World motorcycle test cycle was used as input signal in this vehicle dynamic system. This driving cycle represents the typical speed-time profile used in emissions testing and certification of legally operated motorcycles on roads. This procedure is constructed through steps such as route selection, data collection, and application of appropriate methods to aggregate the data [43]. Figure 6.7 presents the speed-time profile of the WMTC applied in this study [44]. This cycle is divided into 3 parts, each with 3 different characteristics described in Table 6.2. These characteristics summarize the attributes of vehicles running on different road attitudes.

**Table 6.2 Characteristics of WMTC**

WMTC	Time (s)	Distance (km)	Average speed (km/h)	Max. speed (km/h)	Max. acceleration (m/s <sup>2</sup> )	Max. deceleration (m/s <sup>2</sup> )
Part 1	600	4.07	24.4	60.0	2.51	2.00
Part 2	600	9.11	54.7	94.9	2.68	2.02
Part 3	600	15.74	94.4	125.3	1.56	2.00

This dynamic system is constructed based on the real-world motorcycle, Honda Wave 110, with the specifications detailed in Table 6.3. Furthermore, the motorcycle is currently carrying one rider weighing 70 kg, with a height of 165 cm, which is also factored into the aerodynamic resistance calculation.

The simulation diagram is developed for the scenario where the vehicle moves on a level road with a slope of 0. The vehicle speed varies according to WMTC, and the resistance forces change accordingly. As the vehicle is modeled with rear-wheel drive, the resistance was calculated at the rear wheel of the vehicle through dynamic resistance forces. The torque at the wheel, through the primary ratio and final ratio, resulted as the torque at the motor shaft. Here, the torque becomes the input for two different controller methods:

- Case 1: The motor cooling system has been modeled with two ML models, one predicting average motor temperature, and one controlling the coolant flow rate.

This material is reserved for educational use only, not allowed for commercial use.

Forbidden to modify the content, and cite the document when use.

- Case 2: PID is used to control the flow rate, while the ML model, which predicts the average motor temperature, functions as a transfer function to provide feedback to the PID.

**Table 6.3 Specifications of Honda Wave 110**

Overall length	1.897 mm
Overall width	706 mm
Overall height	1.092 mm
Wheelbase	1.227 mm
Minimum ground clearance	135 mm
Maximum weight capacity	134 kg
Maximum weight on rear carrier	3.0 kg
Passenger capacity	Rider and 1 passenger
Gear ratio	1 <sup>st</sup> : 2.615
	2 <sup>nd</sup> : 1.555
	3 <sup>rd</sup> : 1.136
	4 <sup>th</sup> : 0.916
Reduction ratio (primary/final)	4.059/2.642

#### 6.1.4 Memory Optimization for Motor Cooling System

Figure 6.8 depicts a simplified decision tree derived from Figure 6.2. Weight ( $w$ ) represents the signal strength of the neural network, but as information is passed through multiple layers, the neural network needs additional information. Bias ( $b$ ) provides additional characteristics to efficiently transmit information forward. Therefore, the activation function, also known as the transfer function, will take the form of Equation (6.1).

$$T = wf(Tq, IT, FL) + b \quad (6.1)$$

where  $Tq$  is torque of motor,  $IT$  is inlet temperature, and  $FL$  is flow rate of coolant.

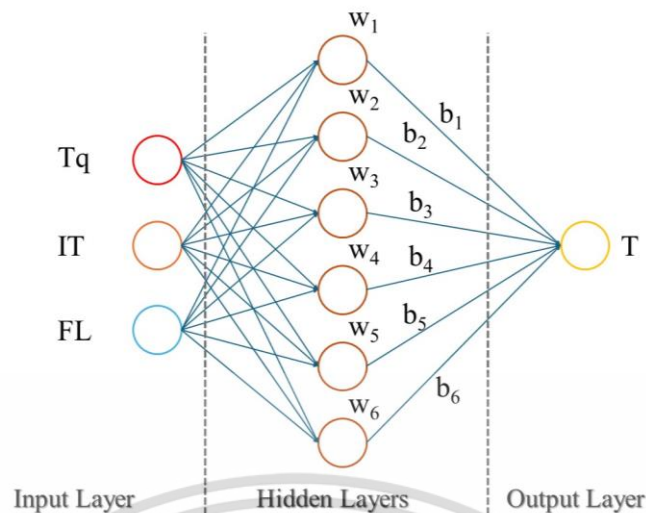


Figure 6.8 Simplified Decision Tree of ML model

In the MATLAB/Simulink environment, the ML model is not the final outcome of this research. A data model is very difficult to transfer due to its large capacity and training characteristics requirements. Nevertheless, transferring the motor cooling system box is still essential if it is to be integrated with other large systems, even EVs model, in the simulation environment. To save capacity for the data model, it would be better if the ML equation could be derived from the motor cooling system and functions like the ML model. Figure 6.9 indicated decision tree of ML equation determination. In this step, input parameters including boundary condition and supervise answer. Boundary condition is optimization condition of motor such as torque of motor, inlet temperature, and flow rate of coolant while supervise answer is average temperature of motor. On the other hand, output parameters are  $a$ ,  $b$ ,  $c$ , and  $d$  of model function.

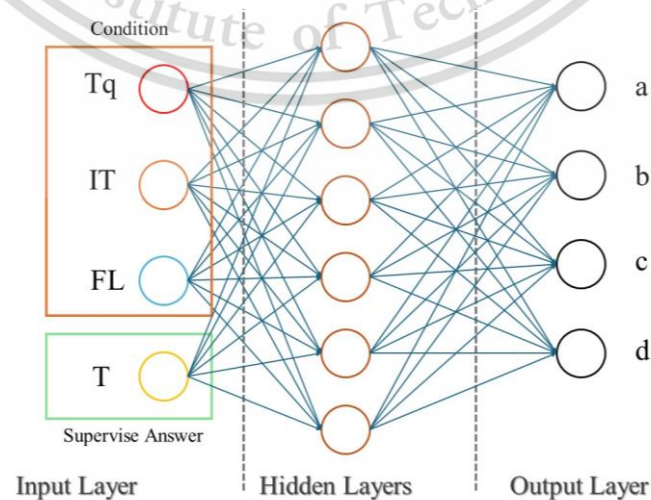


Figure 6.9 Simplified Decision Tree of ML Equation

This material is reserved for educational use only, not allowed for commercial use.

Forbidden to modify the content, and cite the document when use.

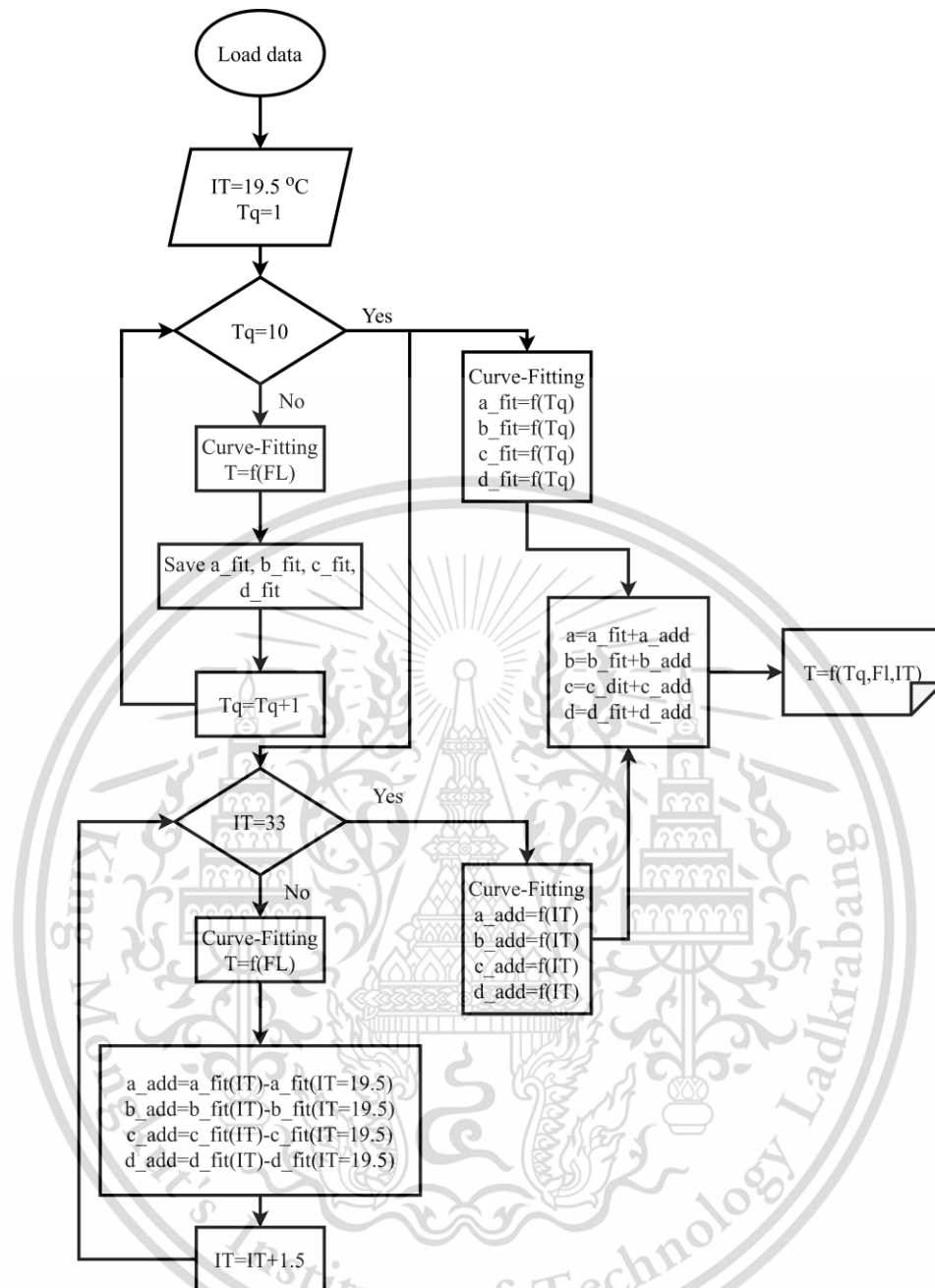


Figure 6.10 Procedure for Determining the Common Equation

The exponential function was chosen as the model function for machine learning because the characteristics of the cooling parameters have an asymptotic trend similar to an exponential function, as shown in Figure 6.11.

Figure 6.10 presents the process of determining the temperature equation relating  $T_q$ ,  $IT$ , and  $FL$ . This process consists of 2 steps:

Step 1:  $IT$  was fixed at 19.5 and  $T_q$  increased from 1 to 10, with each step increasing by 1 Nm. At each increment of  $T_q$ , temperature equation according to the flow rate was found via curve-fitting. When  $T_q=10$ , we obtain 10 equations,  $T=f(FL)$ .

This material is reserved for educational use only, not allowed for commercial use.

Forbidden to modify the content, and cite the document when use.

These equations have a common exponential form due to the choice of activation type as shown in Equation (6.2). Afterwards, the relationship equations between  $T_q$  and the 4 coefficients  $a\_fit$ ,  $b\_fit$ ,  $c\_fit$ , and  $d\_fit$  were determined.

$$T = a\_fit \cdot e^{b\_fit \cdot FL} + c\_fit \cdot e^{d\_fit \cdot FL} \quad (6.2)$$

Step 2:  $T_q$  remains constant at 10 Nm, while  $IT$  rises from 19.5 to 33°C, increasing by 1.5°C in each step. As  $IT$  ascends, the 4 factors  $a\_fit$ ,  $b\_fit$ ,  $c\_fit$ , and  $d\_fit$  also ascend accordingly. This ascent is denoted as  $a\_add$ ,  $b\_add$ ,  $c\_add$ , and  $d\_add$ , respectively. The equation relating  $IT$  and these 4 factors is found via curve-fitting. The general equation is updated as Equation (6.3).

$$T = (a\_fit + a\_add) \cdot e^{(b\_fit + b\_add) \cdot FL} + (c\_fit + c\_add) \cdot e^{(d\_fit + d\_add) \cdot FL} \quad (6.3)$$

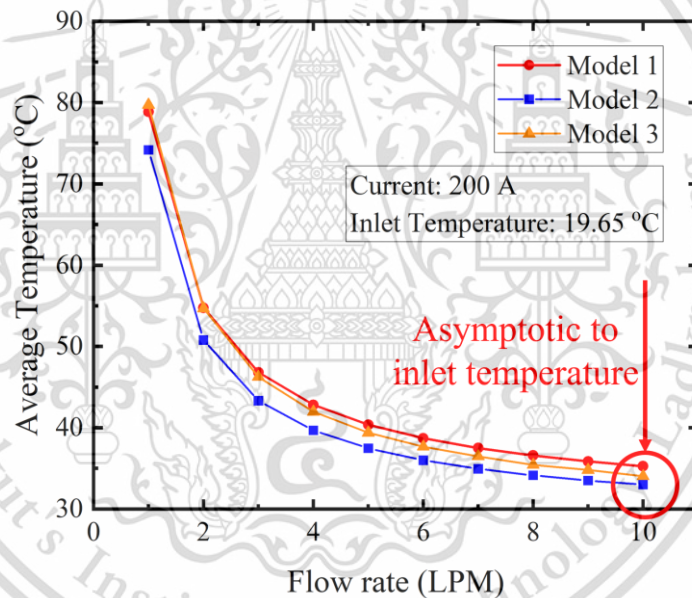


Figure 6.11 Asymptotic Trending of the Cooling Parameters

### 6.1.1 Loss Checking

The validation conditions from Table 4.1 in Chapter 4 are being reused in this test data section of ML model 1. Although accuracy of simulation data has been confirmed in Chapter 4, gradient losses increase within training layers can be decreased accuracy of ML equation. To equation can meet the function of ML model 1, motor cooling system, calibration step should be implemented. After calibrating, ML equation was continuously checked losses base on experimental data, shown in Table 2.1. The schematic of Simulink setup is described in Figure 6.12.

This material is reserved for educational use only, not allowed for commercial use.

Forbidden to modify the content, and cite the document when use.

Table 6.4 Experimental Data Conditions for checking losses of ML Equation

No	Torque of Motor (A)	Inlet Temperature (°C)	Flow Rate (LPM)
1	1.76	19.65	1.9
2	3.08	23.5	2.25
3	4.39	27.5	2.5
4	5.46	31	3

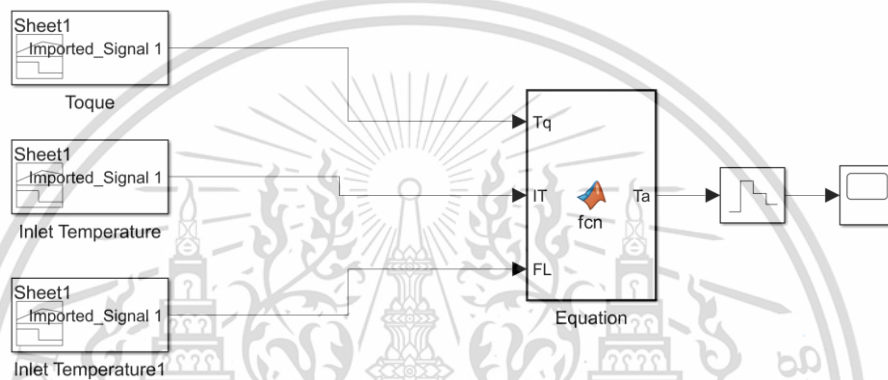
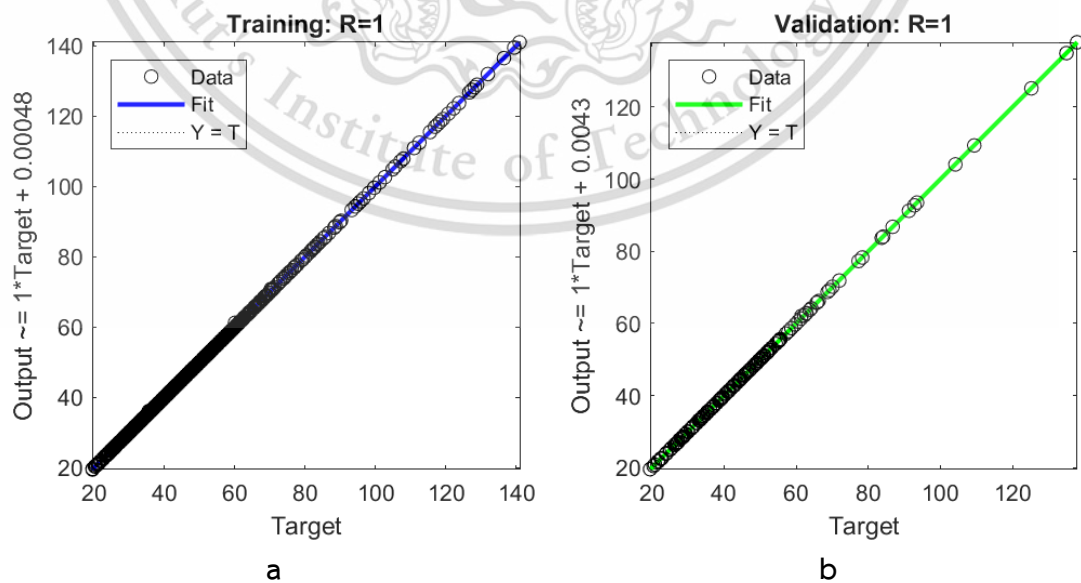


Figure 6.12 Simulink Setup Schematic of Losses Checking

## 6.2 RESULTS AND DISCUSSIONS

### 6.2.1 Accuracy of ML Model 1



This material is reserved for educational use only, not allowed for commercial use.

Forbidden to modify the content, and cite the document when use.

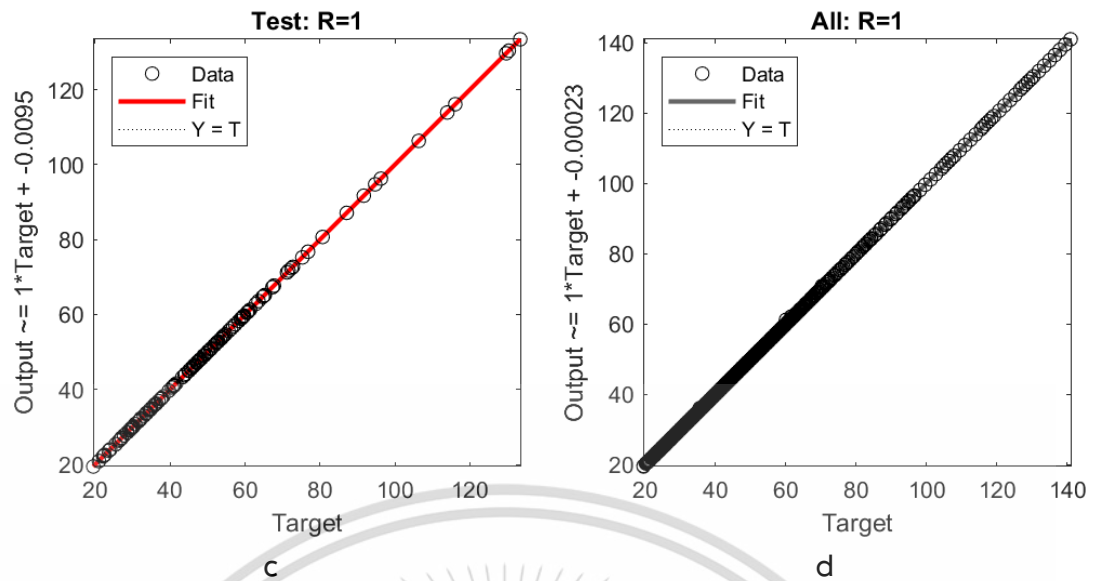


**Figure 6.13 Prediction Accuracy of Motor Temperature**

Training data, validation data, and testing data account for 70%, 15%, and 15% of the database from the simulation, respectively. Figure 6.13 presents the results and accuracy of the training process through the R score of training (a), validation (b), test (c), and all (d) datasets. In this figure, the R scores for the training, validation, and test data achieved a perfect 1. The closer the R score is to 1, the higher the accuracy of the training set [26]. This study indicates the perfect R score of 1 because input parameters for training come from simulation. Simulation is basically calculation of a series of combined formulas. This helps ML model easily to understand and predict data within boundary conditions.

### 6.2.2 Water Utilization

The aim of this results section is to assess pump capacity. Rather than computing and comparing the electrical power supplied to the pump in two different control methods, ML and PID, this section significantly simplifies the results implementation and comparison. Water utilization serves as the focus for calculation and comparison.

In order to evaluate water utilization, flow rate data over time was collected and mathematically calculated its integral. Figure 6.14 and Figure 6.15 display the variations in water flow rate according to the WMTC in ML and PID, respectively.

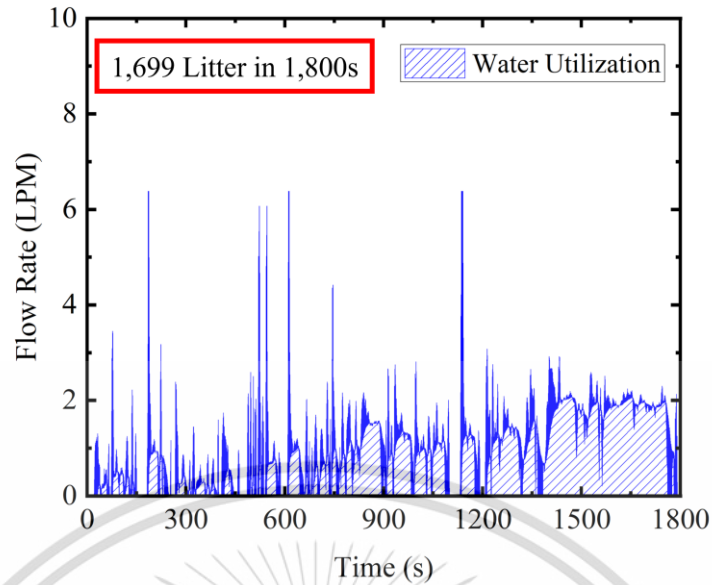


**Figure 6.14 Flow Rate Profile over Time in ML Model Controller**

In Figure 6.14, at the end of the 1800-second cycle, the cooling water usage amounts to 1699 liters, with a maximum flow rate of 6.38 LPM. The peak flow rate of water occurs during specific intervals: from 151s to 183s, 587s to 608s, 1103s to 1132s, and 1194s to 1207s. This explains that the motor torque is high at low RPM, requiring a high electrical current supply to the motor, resulting in an increase in temperature inside the motor winding. At this time, the flow rate must increase quickly to meet the cooling demand.

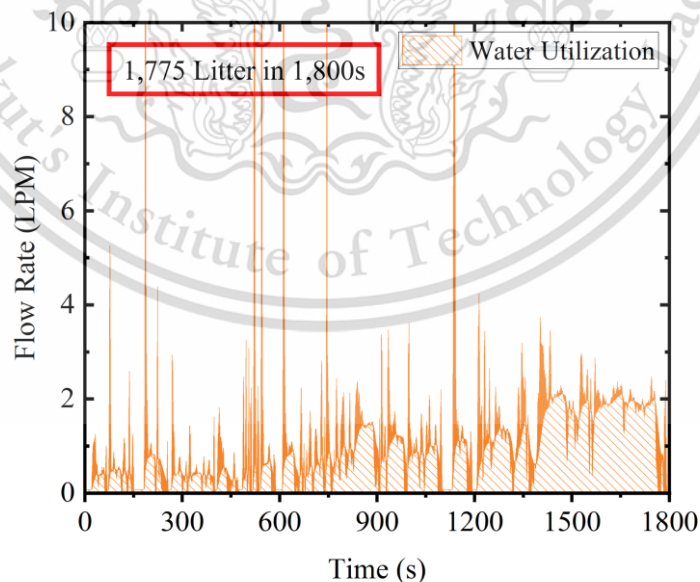


**Figure 6.15 Flow Rate Profile over Time in Logical PID Controller**

In Figure 6.15, the flow rate profile is also mathematically calculated integral over the 1800-second cycle, resulting in 1775 liters, which is 76 liters higher than ML. This material is reserved for educational use only, not allowed for commercial use.

Forbidden to modify the content, and cite the document when use.

accounting for only 4.47 %. This indicates that the pump capacity in the ML controller is lower than in PID; however, the difference is minimal, and water utilization is nearly the same.

The locations of rapid flow rate increase in ML and PID are quite similar. However, the maximum flow rate is 26.47 LPM, which is 20.09 liters higher, or 314.89 % more than ML. This is explained by PID continuously maximizing pump capacity when cooling demands are not met, leading to overtraining of the ML prediction model. Nevertheless, the rapid increase in flow rate and consistent use of high flow rates result in a significant increase in pressure drop while not significantly reducing temperature, as discussed in chapter 4 and chapter 5. This causes a significant loss of pump power, decreasing cooling efficiency. Hence, the optimized control advantage of ML is evident.

### 6.2.3 Optimal ML Equation for Low-memory Processor

To optimize and implement control strategies, finding the equation relating motor temperature to motor torque, inlet temperature, and flow rate is the most feasible approach. Below is the equation determined through machine learning with supervised learning method and exponential activation function.

$$a = 20.18 \cdot Tq - 16.04$$

$$b = -0.96^{Tq} + 0.00066 \cdot IT - 0.01279$$

$$c = 5.08 \times Tq + 0.98 \cdot IT - 35.62$$

$$d = -0.003^{Tq} + 0.00053 \cdot IT - 0.01$$

$$T = a \times e^{b \cdot FL} + c \times e^{d \cdot FL}$$

$$\text{Condition: } FL = [1, 10]; IT = [19.5, 33]; Tq = [1, 10]$$

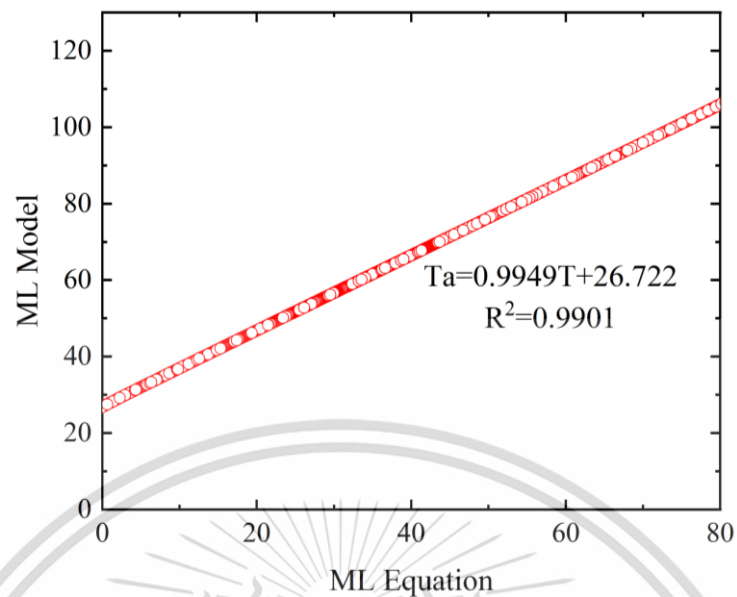


**Figure 6.16 Calibration Equation between ML Model and Equation**

To ensure the accuracy of the equation just found, calibration is performed based on the boundary conditions of the dynamic system in Section 6.2.3. Figure 6.16 illustrates the calibration results with Equation (6.4). This equation was considered the final equation that can be applied in real life. The R score of 0.9901, close to 1, ensuring a match with the original data.

$$T_a = 0.9949 \cdot T + 26.722 \quad (6.4)$$

where  $T_a$  is the adjusted temperature of the motor from calibration,  $T$  is the motor temperature from training process.

#### 6.2.4 Losses Checking of Optimal Equation

Although the R score of the training process is 1 and the strict validation, gradient losses can be increased in the equation determination steps. Therefore, it is necessary to check equation losses based on original data, experimental data was used in the validation step. From this, equation accuracy will be evaluated, specific values were indicated in Table 6.5.

**Table 6.5 Losses Checking of Optimal Equation**

R score	Maximum AE (°C)	Maximum RE (%)
0.9994	5.47	17.09

Although AE and RE are relatively high at 5.47°C and 17.09%, respectively, the R score of 0.9998 implies that the ML equation closely aligns with the majority of the test results and only a few test cases deviate from this equation. Nevertheless, this result also demonstrates that ML has the potential for application in cooling system control and optimization for low-memory embedded processors. The remaining cases with errors can be adjusted using certain conditional functions.

The R score of the calibration step being lower than the R score of the losses checking step can be explained by two points:

- Calibration with the ML model was conducted on 1,000 cases, while losses checking with the experiment was only implemented on 64 cases.
- A limitation of using machine learning for prediction is that accuracy decreases when boundary conditions move far from the actual experimental data.

Additionally, the ML model and ML equation were trained for specific boundary conditions, and accuracy will decrease significantly if the working conditions exceed these boundaries. However, this model was integrated and designed to cover the full range of possible working conditions.

Moreover, ML equation is fundamental step to develop deep neural network (DNN) model. From this, it is easy to derive the equation by input matrix includes boundary conditions and supervise answer and the output data includes parameters *a*, *b*, *c*, and *d*. This approach allows for quickly inferring equations for different motors, higher power motors, and even EV motors. However, this direction requires collecting extensive data from many types of motors.

## CHAPTER 7

### CONCLUSIONS AND RECOMMENDATIONS

#### 7.1 CONCLUSIONS

This study has been divided into several different parts to separately evaluate various aspects of the cooling system.

The assessment of factors impacting the cooling process of the WJ implemented for SynRM has been explored. Drawing from simulation and experimental outcomes, the main conclusions are summarized as follows:

- The WJ has proven its cooling effectiveness by considerably reducing the temperature of the SynRM winding and jacket. Moreover, the simulation results have been gathered and organized for input parameters of the simulation.
- Temperature fluctuations stem from the phase shift of three-phase alternating current. Consequently, as the peak current increases, temperature oscillations also rise, but they decrease with increasing flow rate. These temperature oscillations present the next challenge when seeking to increase motor torque, as they directly influence the motor lifespan.
- As the motor torque increases, the supplied current needs to rise accordingly, resulting in a rapid increase in the temperature within the motor winding, necessitating cooling.

In this study, the validation step is carried out comprehensively with three different aspects of validation. The conclusions are summarized as follows:

- Time-dependent validation has demonstrated that the temperature variations between simulation and experiment tend to be similar and stable at approximately the same temperature levels.
- Steady-state validation was conducted with 64 cases, with the largest RE being 6.77%. The stable temperatures of the simulation and experiment were relatively close to each other.

- Temperature distribution showed a significant correlation between simulation and experiment in the increase of temperature from the inlet to the outlet.

When comparing the different WJs to each other, the conclusions are summarized as follows:

- Increasing flow rate reduced the maximum temperature, but with diminishing returns beyond a certain value. To balance cooling capacity and power consumption, a specific threshold for the flow rate should be set and not exceeded.
- A shorter water path and independent channel reduce pressure drop, save pump capacity
- A serpentine water path and water content exchange enhanced the apparent heat transfer coefficient, reducing the maximum temperature.

The ML model was trained with high accuracy, consistently achieving perfect R score of 1. Unlike to PID, ML model can directly select optimal flow rate to quicky control and effective cooling capacity. This study has proven the applicability of using ML models in the role of cooling system control.

To optimize capacity for interacting with other models, even EVs model, the equation has been found and calibrated with high accuracy.

Finally, the losses of the final equation were checked against experimental data reserved for the validation step, yielding an R score of 0.994, which is higher than the R score obtained during calibration with the ML model (0.9901). This indicates that the equation aligns well with the experimental data, and accuracy gradually decreases as the boundary conditions move away from the actual data.

## 7.2 DEVELOPMENT DIRECTIONS

**Using a DNN to derive equations:** In this approach, a DNN model is generated with boundary conditions and the temperature matrix as input data, and parameters *a*, *b*, *c*, and *d* as output data. This allows for the quick derivation of equations for different motors, higher power motors, and even EV motors. However, this direction requires collecting extensive data from many types of motors.

## BIBLIOGRAPHY AND REFERENCES

- [1] E. F. I. Raj, M. Appadurai, S. Darwin, and M. C. Thanu. 2022. "Detailed study of efficient water jacket cooling system for induction motor drive used in electric vehicle". **Int. J. Interact. Des. Manuf.** 17: 1277-1288.
- [2] M. Cavazzuti, G. Gaspari, S. Pasquale, and E. Stalio. 2019. "Thermal management of a Formula E electric motor: Analysis and optimization". **Appl Therm Eng.** 157: 113733.
- [3] P. S. Wu *et al.* 2019. "Heat transfer and thermal management of interior permanent magnet synchronous electric motor". **Inventions.** 4(4): 69.
- [4] P. Liang, F. Chai, K. Shen, and W. Liu. 2019. "Thermal design and optimization of a water-cooling permanent magnet synchronous in-wheel motor" 1-6. In IEEE.
- [5] X. Wang *et al.* 2022. "A critical review on thermal management technologies for motors in electric cars". **Appl Therm Eng.** 201: 117758.
- [6] H. Heidari *et al.* 2021. "A Review of Synchronous Reluctance Motor-Drive Advancements". **Sustainability.** 13(2): 729.
- [7] N. Bedetti, S. Calligaro, and R. Petrella. 2016. "Stand-Still Self-Identification of Flux Characteristics for Synchronous Reluctance Machines Using Novel Saturation Approximating Function and Multiple Linear Regression". **IEEE Trans Ind Appl.** 52(4): 3083-3092.
- [8] D. Gerling. 2014. **Electrical Machines: Mathematical Fundamentals of Machine Topologies.** Springer Berlin Heidelberg.
- [9] B. Kerdsup and S. Karukanan. 2022. "Design of Motor Characteristic Testbed for Permanent-Magnet Assisted Synchronous Reluctance Motor" 1-4. In IEEE.
- [10] E. Gundabattini, A. Mystkowski, R. Raja Singh, and S. D. Gnanaraj. 2021. "Water cooling, PSG, PCM, Cryogenic cooling strategies and thermal analysis (experimental and analytical) of a Permanent Magnet Synchronous Motor: a review". **Sadhana.** 46(3): 124.
- [11] M. H. Gordon, M. B. Stewart, B. King, J. C. Balda, and K. J. Olejniczak. 1995. "Numerical optimization of a heat sink used for electric motor drives" 967-970. In 2.

This material is reserved for educational use only, not allowed for commercial use.

Forbidden to modify the content, and cite the document when use.

- [12] S. Pickering, P. Wheeler, F. Thovex, and K. Bradley. 2006. "Thermal Design of an Integrated Motor Drive" 4794-4799. In
- [13] H. Li. 2010. "Cooling of a permanent magnet electric motor with a centrifugal impeller". **International Journal of Heat and Mass Transfer**. 53(4): 797-810.
- [14] S. Ding, J. Liu, and L. Zhang. 2017. "Fan characteristics of the self-support components of rotor ends and its performance matching". **International Journal of Heat and Mass Transfer**. 108: 1917-1923.
- [15] C. Kim, K.-S. Lee, and S.-J. Yook. 2016. "Effect of air-gap fans on cooling of windings in a large-capacity, high-speed induction motor". **Appl Therm Eng**. 100: 658-667.
- [16] W. Chen, Y. Ju, D. Yan, L. Guo, Q. Geng, and T. Shi. 2019. "Design and optimization of dual-cycled cooling structure for fully-enclosed permanent magnet motor". **Appl Therm Eng**. 152: 338-349.
- [17] F. Marcolini, G. De Donato, F. G. Capponi, and F. Caricchi. 2021. "Direct Oil Cooling of End-Windings in Torus-Type Axial-Flux Permanent-Magnet Machines". **IEEE Trans Ind Appl**. 57(3): 2378-2386.
- [18] P. Lindh *et al.* 2017. "Direct Liquid Cooling Method Verified With an Axial-Flux Permanent-Magnet Traction Machine Prototype". **IEEE Transactions on Industrial Electronics**. 64(8): 6086-6095.
- [19] B. Prieto, M. Satrustegui, I. Elósegui, and N. Gil-Negrete. 2020. "Multidisciplinary analysis of a 750 kW PMSM for marine propulsion including shock loading response". **IET Electr Power Appl**. 14(10): 1933-1943.
- [20] B. Silwal, A. H. Mohamed, J. Nonneman, M. De Paepe, and P. Sergeant. 2019. "Assessment of different cooling techniques for reduced mechanical stress in the windings of electrical machines". **Energies**. 12(10): 1967.
- [21] M. Al-Gabalawy. 2021. "Advanced machine learning tools based on energy management and economic performance analysis of a microgrid connected to the utility grid". **International Journal of Energy Research**. 46: 24667-24667.
- [22] L. Zhao, W. Yao, Y. Wang, and J. Hu. 2020. "Machine Learning-Based Method for Remaining Range Prediction of Electric Vehicles". **IEEE Access**. 8: 212423-212441.

- [23] C. E. Sunal, V. Dyo, and V. Velisavljevic. 2022. "Review of Machine Learning Based Fault Detection for Centrifugal Pump Induction Motors". **IEEE Access**. 10: 71344-71355.
- [24] H. Sauerland, A. Miyamoto, A. Ohazulike, H. Xu, and R. W. De Doncker. 2022. "Tn, rom, ml, pinns-four approaches for real-time temperature estimation in electric motors in comparison" In Scipedia S.L.
- [25] W. Kirchgassner, O. Wallscheid, and J. Bocker. 2021. "Estimating Electric Motor Temperatures with Deep Residual Machine Learning". **IEEE Trans Power Electron**. 36(7): 7480-7488.
- [26] Y. Wang, M. Li, R. Wang, G. Hou, and W. Chang. 2023. "Design and optimization of driving motor cooling water pipeline structure based on a comprehensive evaluation method and CNN-PSO". **e-Prime - Adv. Elec. Eng. Elec. Energy**. 3: 100125.
- [27] M. Weber, F. He, M. Weigold, and E. Abele. 2021. **Development of a Temperature Strategy for Motor Spindles with Synchronous Reluctance Drive Using Multiple Linear Regression and Neural Network**. Springer Nature.
- [28] D. Schramm, M. Hiller, and R. Bardini. 2014. **Vehicle Dynamics: Modeling and Simulation**. Springer Berlin Heidelberg.
- [29] R. N. Jazar. 2008. **Vehicle dynamics : theory and applications**. New York. Springer.
- [30] T. D. Gillespie, S. Taheri, C. Sandu, and B. L. Duprey. 2021. **Fundamentals of vehicle dynamics**. Warrendale, Pennsylvania. SAE International.
- [31] X. Yang, A. Fatemi, T. Nehl, L. Hao, W. Zeng, and S. Parrish. 2019. "Comparative study of three stator cooling jackets for electric machine of mild hybrid vehicle" 1202-1209. In IEEE.
- [32] S. Hirasawa, T. Kawanami, and K. Shirai. 2016. "Efficient cooling system using electrocaloric effect". **Journal of Electronics Cooling and Thermal Control**. 6(2): 78-87.
- [33] I. Y. Braslavsky, V. Metelkov, D. Esaulkova, and A. Kostylev. 2018. "Simplified method of taking into account temperature fluctuations influence on durability of induction motors stator winding insulation" 1-4. In IEEE.

- [34] R. Smith, A. Tikadar, S. Kumar, and Y. Joshi. 2022. "Evaporative Cooling of High Power Density Motors: Design and Analysis" 1-8. In IEEE Computer Society.
- [35] C. Chu, Y. Huang, and F. Peng. 2023. "Comparative Analysis of Surface-Attached Cooling Structure for Efficient Thermal Management of SPMM-TW". **IEEE Trans. Transp. Electr.** 9(2): 2398-2408.
- [36] H. Vansompel and P. Sergeant. 2020. "Extended End-Winding Cooling Insert for High Power Density Electric Machines with Concentrated Windings". **IEEE Trans Energy Convers.** 35(2): 948-955.
- [37] Y. Wan, Q. Li, J. Guo, and S. Cui. 2020. "Thermal analysis of a Gramme-ring-winding high-speed permanent-magnet motor for pulsed alternator using CFD". **IET Electr Power Appl.** 14(11): 2111-2118.
- [38] H. Wang, T. Tao, J. Xu, X. Mei, X. Liu, and P. Gou. 2020. "Cooling capacity of a novel modular liquid-cooled battery thermal management system for cylindrical lithium ion batteries". **Appl Therm Eng.** 178: 115591.
- [39] B. Zhang, R. Qu, X. Fan, and J. Wang. 2015. "Thermal and mechanical optimization of water jacket of permanent magnet synchronous machines for EV application" 1329-1335. In IEEE.
- [40] G. Venturini, G. Volpe, M. Villani, and M. Popescu. 2020. "Investigation of cooling solutions for hairpin winding in traction application" 1573-1578. In Institute of Electrical and Electronics Engineers Inc.
- [41] P. M. Lindh *et al.* 2016. "Direct liquid cooling in low-power electrical machines: Proof-of-concept". **IEEE Trans Energy Convers.** 31(4): 1257-1266.
- [42] V. Kotu and B. Deshpande. 2019. **Chapter 4 - Classification**. Morgan Kaufmann.
- [43] M. Sithanathan and R. Kumar. 2021. "A framework for development of real-world motorcycle driving cycle in India". **Proceedings of the Institution of Mechanical Engineers, Part D: Journal of Automobile Engineering.** 235(6): 1497-1515.
- [44] H. Steven. 2002. "Worldwide harmonised motorcycle emissions certification procedure". **Institute for Vehicle Technology**.

## Appendix A

## ICOME 2023 CONFERENCE AND CERTIFICATE



This material is reserved for educational use only, not allowed for commercial use.

Forbidden to modify the content, and cite the document when use.

## Appendix B

# PUBLICATION

Journal of Research and Applications in Mechanical Engineering  
 ISSN: 2229-2152 (Print); 2697-424x (Online)  
 (2024) Vol. 12, No. 1, Paper No. JRAME-24-12-010  
 [DOI: 10.14456/jrame.2024.10]



### Research Article

## Efficiency Evaluation on Cooling Behavior of Water-Cooling Jacket for Synchronous Reluctance Motor

K.H. Nguyen<sup>1</sup>  
 M. Masomtob<sup>2,\*</sup>  
 B. Kerdsup<sup>3</sup>  
 S. Karukanan<sup>4</sup>  
 P. Champa<sup>5</sup>  
 T.D. Pham<sup>6</sup>  
 S. Hirai<sup>4</sup>  
 C.T. Vo<sup>4</sup>  
 P. Kummool<sup>6</sup>

<sup>1</sup> Department of Mechanical Engineering, School of Engineering, King Mongkut's Institute of Technology Ladkrabang, Bangkok, 10520, Thailand

<sup>2</sup> National Energy Technology Center, National Science and Technology Development Agency, Pathum Thani, 12120, Thailand

<sup>3</sup> National Electronics and Computer Technology Center, National Science and Technology Development Agency, Pathum Thani, 12120, Thailand

<sup>4</sup> School of Engineering, Tokyo Institute of Technology, Tokyo, 152-8552, Japan

<sup>5</sup> Faculty of Automotive Engineering Technology, Industrial University of Ho Chi Minh City, Ho Chi Minh City, 727900, Vietnam

<sup>6</sup> International Academy of Aviation Industry, King Mongkut's Institute of Technology Ladkrabang, Bangkok, 10520, Thailand

Received 30 August 2023  
 Revised 13 November 2023  
 Accepted 22 November 2023

### Abstract:

*This study presents the cooling efficiency after installing a water-cooling jacket for a 3-kW synchronous reluctance motor of an electric motorcycle and the factors influencing its thermal behavior by experimental and simulation approaches. The testing process was conducted as a method to collect input parameters and validate the results of the computing simulation. The simulation procedure used the step running technique to evaluate two different water-path models. The findings indicated that the maximum temperature of the stator winding and jacket cover decreased by 19.12 °C and 16.07 °C, respectively, following the installation of the water jacket and operation at a low flow rate with a current supply of 200 A. Furthermore, increasing the water flow rate leads to a substantial decrease in maximum temperature before a certain flow rate; 2 liters per minute (LPM) was chosen as the optimal rate. Temperature fluctuations exhibit an upward trend up to 1.85 °C with the higher supplied currents but drop with a higher flow rate. In addition, the motor maximum temperature in the long water-path jacket (LWJ) model was lower than in the short water-path jacket (SWJ) model due to the higher heat transfer coefficient (HTC).*

**Keywords:** Synchronous reluctance motor, Electric motorcycle, Water-Cooling jacket, Time-Dependent temperature

### 1. Introduction

Facing the depletion risk of fossil fuel resources, the world's attitude towards the internal combustion engine has changed. Given this situation, electric vehicle (EVs) was being considered as a potential replacement for vehicles powered by ICE [1]. The current state of EVs still offers opportunities for improvement, with vehicle performance being a central focus of research and development efforts [2-4]. According to Wang et al. [5], high power density in

\* Corresponding author: M. Masomtob  
 E-mail address: manop.mas@entec.or.th



**Appendix C**  
**COMPARISON TABLE BETWEEN ML EQUATION AND**  
**EXPERIMENTAL DATA**

No	Torque (Nm)	Inlet Temperature (°C)	Flow Rate (LPM)	Motor Temperature (°C)	
				Experimental Data	ML Equation
1	1.763584	19.65	1.9	25.99	22.445197970
2	3.081949	19.65	1.9	31.15	32.566225280
3	4.387849	19.65	1.9	37.50	42.291352388
4	5.461865	19.65	1.9	44.66	50.137484657
5	1.763584	23.5	1.9	29.68	26.135494935
6	3.081949	23.5	1.9	34.77	36.240347972
7	4.387849	23.5	1.9	41.64	45.970476742
8	5.461865	23.5	1.9	48.62	53.829100773
9	1.763584	27.5	1.9	33.20	30.000125386
10	3.081949	27.5	1.9	38.55	40.08788065
11	4.387849	27.5	1.9	45.43	49.823093772
12	5.461865	27.5	1.9	52.84	57.694675578
13	1.763584	31	1.9	37.10	33.407368116
14	3.081949	31	1.9	42.37	43.479915954
15	4.387849	31	1.9	49.15	53.219483332
16	5.461865	31	1.9	55.98	61.102385615
17	1.763584	19.65	2.15	25.80	21.818230267
18	3.081949	19.65	2.15	30.59	31.095143982
19	4.387849	19.65	2.15	37.21	39.979917234
20	5.461865	19.65	2.15	44.58	47.137953870
21	1.763584	23.5	2.15	29.62	25.495883894
22	3.081949	23.5	2.15	34.47	34.750112784
23	4.387849	23.5	2.15	41.24	43.636197119
24	5.461865	23.5	2.15	48.38	50.804793305

This material is reserved for educational use only, not allowed for commercial use.

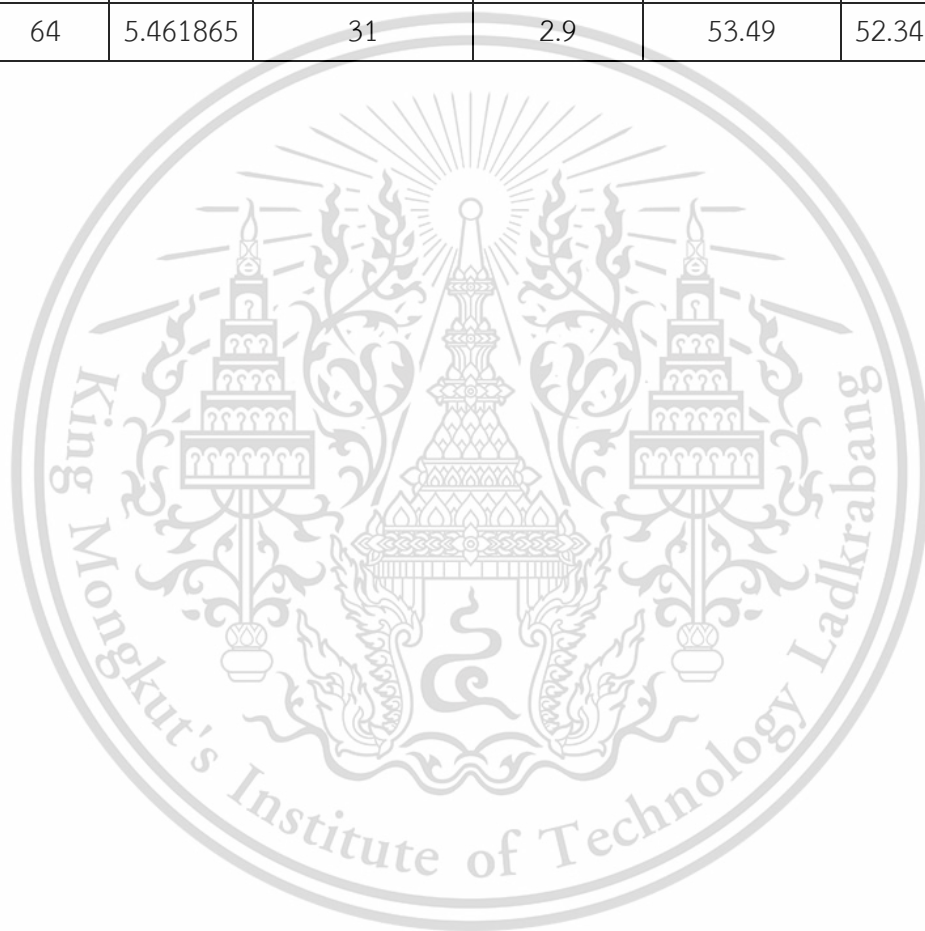
Forbidden to modify the content, and cite the document when use.

25	1.763584	27.5	2.15	33.02	29.351312744
26	3.081949	27.5	2.15	38.10	38.581572697
27	4.387849	27.5	2.15	44.89	47.468851201
28	5.461865	27.5	2.15	51.50	54.648371822
29	1.763584	31	2.15	36.86	32.753833953
30	3.081949	31	2.15	42.33	41.962783950
31	4.387849	31	2.15	48.46	50.850965681
32	5.461865	31	2.15	55.90	58.040005783
33	1.763584	19.65	2.4	25.65	21.333597301
34	3.081949	19.65	2.4	29.42	29.958449668
35	4.387849	19.65	2.4	35.97	38.192299372
36	5.461865	19.65	2.4	44.50	44.817463502
37	1.763584	23.5	2.4	28.66	24.998686457
38	3.081949	23.5	2.4	34.42	33.594492591
39	4.387849	23.5	2.4	38.85	41.826103281
40	5.461865	23.5	2.4	47.16	48.460006830
41	1.763584	27.5	2.4	32.68	28.844976104
42	3.081949	27.5	2.4	36.74	37.410082319
43	4.387849	27.5	2.4	44.81	45.639134502
44	5.461865	27.5	2.4	48.96	52.282041093
45	1.763584	31	2.4	36.86	32.242818956
46	3.081949	31	2.4	41.96	40.780622748
47	4.387849	31	2.4	47.53	49.007240253
48	5.461865	31	2.4	54.02	55.657959446
49	1.763584	19.65	2.9	24.94	20.672546314
50	3.081949	19.65	2.9	29.15	28.401992566
51	4.387849	19.65	2.9	34.91	35.734745839
52	5.461865	19.65	2.9	44.30	41.620968842
53	1.763584	23.5	2.9	28.59	24.312953309
54	3.081949	23.5	2.9	34.09	32.001307945
55	4.387849	23.5	2.9	38.71	39.325352048

This material is reserved for educational use only, not allowed for commercial use.

Forbidden to modify the content, and cite the document when use.

56	5.461865	23.5	2.9	45.29	45.217169558
57	1.763584	27.5	2.9	32.38	28.141372380
58	3.081949	27.5	2.9	36.52	35.786227836
59	4.387849	27.5	2.9	42.39	43.100840326
60	5.461865	27.5	2.9	48.51	48.998321573
61	1.763584	31	2.9	36.05	31.530182846
62	3.081949	31	2.9	40.57	39.136295611
63	4.387849	31	2.9	46.93	46.442331688
64	5.461865	31	2.9	53.49	52.344642743



This material is reserved for educational use only, not allowed for commercial use.

Forbidden to modify the content, and cite the document when use.

# CURICULUM VITAE

**Name** Mr. Hoang Khan Nguyen  
**Date of Birth** May 21, 2000, in Vietnam

## Educational Background:

2018: Engineer degree in Automotive Engineering Technology, Industrial University of Ho Chi Minh City, Vietnam.

2022: Master of Engineering in Automotive and Advanced Transportation Engineering (A2TE), King Mongkut's Institute of Technology Ladkrabang.

**Scholarship** Received a scholarship from the Monozukuri degree project. Received full refund scholarship for a master's degree at TAIST Tokyo Tech.

## Work Experience

2022 Automotive Engineer Intern at CarTek Services Trading Company Limited, Vietnam

2023 Research Intern at National Chung Cheng University (CCU), Chiayi, Taiwan

## Research Achievements

2023 K H Nguyen, M Masomtob, B Kerdsup, S Karukanan, P Champa, T D Pham, S Hirai, C T Vo, P Kumool, and C Charoenphonphanich. Efficiency evaluation on cooling behavior of water-cooling jacket for synchronous reluctance motor. Journal of Research and Application in Mechanical Engineering (2024) Vol. 12, No. 1.